Determination of Electrochemical Performance and Thermo-Mechanical-Chemical Stability of SOFCs from Defect Modeling

FINAL REPORT

Reporting Period Start Date: Janaury 1, 2003

Reporting Period End Date: December 31, 2006

Eric D. Wachsman and Keith L. Duncan

January, 2007

CONTRACT NUMBER: DE-FC26-02NT41562

Department of Materials Science and Engineering, University of Florida

Gainesville, FL, 32611-6400

Phone: (352) 846-2991; Fax: (352) 846-0326; E-mail: ewach@mse.ufl.edu

DOE Project Manager: Travis Schultz

Phone: (304) 285-1370; E-mail: Travis.Shultz@netl.doe.gov

DISCLAIMER

"This report was prepared as an account of work sponsored by an agency of the United States Government. Neither the United States Government nor any agency thereof, nor any of their employees, makes any warranty, express or implied, or assumes any legal liability or responsibility for the accuracy, completeness, or usefulness of any information, apparatus, product, or process disclosed, or represents that its use would not infringe privately owned rights. Reference herein to any specific commercial product, process, or service by trade name, trademark, manufacturer, or otherwise does not necessarily constitute or imply its endorsement, recommendation, or favoring by the United States Government or any agency thereof. The views and opinions of authors expressed herein do not necessarily state or reflect those of the United States Government or any agency thereof."

ABSTRACT

This research was focused on two distinct but related issues. The first issue concerned using defect modeling to understand the relationship between point defect concentration and the electrochemical, thermo-chemical and mechano-chemical properties of typical solid oxide fuel cell (SOFC) materials. The second concerned developing relationships between the microstructural features of SOFC materials and their electrochemical performance.

To understand the role point defects play in ceramics, a coherent analytical framework was used to develop expressions for the dependence of thermal expansion and elastic modulus on point defect concentration in ceramics. These models, collectively termed the continuum-level electrochemical model (CLEM), were validated through fits to experimental data from electrical conductivity, I-V characteristics, elastic modulus and thermo-chemical expansion experiments for (nominally pure) ceria, gadolinia-doped ceria (GDC) and yttria-stabilized zirconia (YSZ) with consistently good fits. The same values for the material constants were used in all of the fits, further validating our approach. As predicted by the continuum-level electrochemical model, the results reveal that the concentration of defects has a significant effect on the physical properties of ceramic materials and related devices.

Specifically, for pure ceria and GDC, the elastic modulus decreased while the chemical expansion increased considerably in low partial pressures of oxygen. Conversely, the physical properties of YSZ remained insensitive to changes in oxygen partial pressure within the studied range. Again, the findings concurred exactly with the predictions of our analytical model. Indeed, further analysis of the results suggests that an increase in the point defect content weakens the attractive forces between atoms in fluorite-structured oxides.

The reduction treatment effects on the flexural strength and the fracture toughness of pure ceria were also evaluated at room temperature. The results reveal that the flexural strength decreases significantly after heat treatment in very low oxygen partial pressure environments; however, in contrast, fracture toughness is increased by 30–40% when the oxygen partial pressure was decreased to 10^{-20} to 10^{-22} atm range. Fractographic studies show that microcracks developed at 800 ^{o}C upon hydrogen reduction are responsible for the decreased strength.

To understand the role of microstructure on electrochemical performance, electrical impedance spectra from symmetric LSM/YSZ/LSM cells was de-convoluted to obtain the key electrochemical components of electrode performance, namely charge transfer resistance, surface diffusion of reactive species and bulk gas diffusion through the electrode pores. These properties were then related to microstructural features, such as triple-phase boundary length and tortuosity.

From these experiments we found that the impedance due to oxygen adsorption obeys a power law with pore surface area, while the impedance due to charge transfer is found to obey a power-law with respect to triple phase boundary length. A model based on kinetic theory explaining the power-law relationships observed was then developed. Finally, during our EIS work on the symmetric LSM/YSZ/LSM cells a technique was developed to improve the quality of high-frequency impedance data and their subsequent de-convolution.

TABLE OF CONTENTS

LIST OF GRAPHICAL MATERIALS

LIST OF FIGURES

LIST OF TABLES

INTRODUCTION

Despite the many advances made in the development of solid oxide fuel cells (SOFCs), there are significant issues to address in order to achieve large-scale commercialization. To wit, SOFC failure analysis, cathode polarization, and interaction with power conditioning systems and various loads are some of the macro-issues that are yet to be resolved satisfactorily. Accordingly, much research is being conducted to address these problems.

When examined closely and carefully, however, a common thread, linking many of these areas, appears. Perhaps not surprisingly, that thread is the concentration of point defects. Point defect concentration underpins numerous SOFC performance criteria. The variation in strength as a function of oxygen partial pressure, P_{O_2}, or an electric voltage of SOFC components is governed by point defect concentration. The strength of a component depends on the lattice constant of the material and the lattice constant of a material changes with the concentration of point defects. The (ionic and electronic) conductivity of an SOFC component (which further relates to other properties such as electrochemical efficiency) also varies with the point defect concentration. The transient response of an SOFC to changes in load, variations in operating conditions (e.g., P_{O_2} of the fuel mixture), or current/voltage ripples from the power electronics depends on how rapidly the defects in the SOFC components can reorganize themselves, i.e., adjust to new operating conditions.

For a more meaningful discussion, let us consider the thermo-mechanical and thermo-chemical stability of SOFCs. Thermo-mechanical stability depends on the thermo-elastic properties of their mixed ionic-electronic conductor (MIEC) components. An important facet of thermo-mechanical stability is thermal cycling, which concerns the mechanical stresses and strains that result from repetitive heating (startup) and cooling (shutoff). This problem is exacerbated by expansion mismatches between SOFC components. The effect of thermal cycling is manifested by the volume expansion, $\Delta V/V$, which is defined as

$$\Delta V/V = \gamma \Delta T \tag{1}$$

where V is volume, ΔV is the change in volume for a change in temperature, ΔT, and γ is the coefficient of expansion. However, $V \propto a^3$, where a is the lattice parameter of the MIEC. Typically, a is a function of the ionic species concentration, c_{ion}, e.g., oxygen vacancies, thus,

$$\Delta V/V \propto \Delta a/a \propto f(c_{ion}) \tag{2}$$

where, f is some function of c_{ion}. Hence, insight into the effects of thermal cycling on volume expansion, and more so the mismatch between components of the SOFC, is dependent on a knowledge of c_{ion} and its effect on a. Significantly, if c_{ion} is also a function of position (e.g., from the *high* P_{O_2} cathode side to the *low* P_{O_2} anode side of the SOFC) the volume expansion will likewise vary with position in the components of the SOFC. Moreover, knowing the relationship between the volume expansion and the defect concentration will improve the tracking of the sources of failure in the failure analysis models used by the national laboratories and SECA industrial teams.

The chemical stability of the SOFC components concerns deleterious chemical *inter*-reactions between SOFC components and the environment and *intra*-reactions between the SOFC components. Both are dependent on the concentration of point defects. An example of the latter, reported in the literature[1], is (at typical SOFC operating temperatures) the reaction between cubic stabilized zirconia (CSZ) electrolytes and lanthanum strontium manganate (LSM) cathodes, which occurs as follows:

$$\underset{\text{cathode}}{La_{1-y}Sr_yMnO_3} + \delta\underset{\text{zirconia electrolyte}}{Zr_{Zr}^{\times}} + 2\delta O_O^{\times} + \underset{\text{gas phase}}{\tfrac{3}{4}\delta O_2} \rightarrow \underset{\text{weakened cathode}}{La_{1-y-\delta}Sr_yMnO_3} + \underset{\text{secondary phase}}{\tfrac{\delta}{2}La_2Zr_2O_7} + \tfrac{3}{2}\delta V_O^{\bullet\bullet} + 3\delta e' \tag{3}$$

As written, Eq. (3) argues that the presence of charge carriers (oxygen vacancies and electrons) plays a vital role in the formation of lanthanum zirconate from CSZ and LSM. Specifically, it shows that the rate of formation of lanthanum zirconate can be controlled by electron concentration at the electrolyte-cathode interface. However, the supply of electrons to the electrolyte-cathode interface (i.e., the current density) is controlled by the load resistance. Hence, the rate of lanthanum zirconate formation can be controlled through the load. This has already been proven experimentally[2], but for commercialization it is desirable to have a way to

predict the rate of lanthanum zirconate formation so that the useful life of the SOFC is determinable.

Another example is the issue of cathode polarization. Again, using resistor networks to represent the electrochemical response of SOFC components (currently the state-of-the-art) obviates the non-linear (i.e., non-ohmic) behavior of SOFC components. Typically this leads to an *underestimation* of polarization effects in SOFC components, which then causes an *overestimation* of their performance and the blame to be attributed to a component. For example, Fig. 1 shows a comparison of current and power efficiencies calculated from models with different assumptions for a doped ceria electrolyte. The figure shows that using fixed boundary conditions and assuming a linear Galvani potential leads to an overestimation of both current and power efficiencies. Assuming a linear potential ignores the efficiency sapping effects of mixed conduction and using *fixed* (i.e., independent of potential) boundary concentrations reduces the effects of changing concentration gradients. Consequently, when these assumptions are removed the calculated efficiencies are smaller. These results emphasize the importance of using the correct electrochemical model as the basis for computation of relevant properties.

In light of the above examples, it is evident that a clear understanding of the relationships between the point defect concentration, the operating conditions of an SOFC and relevant

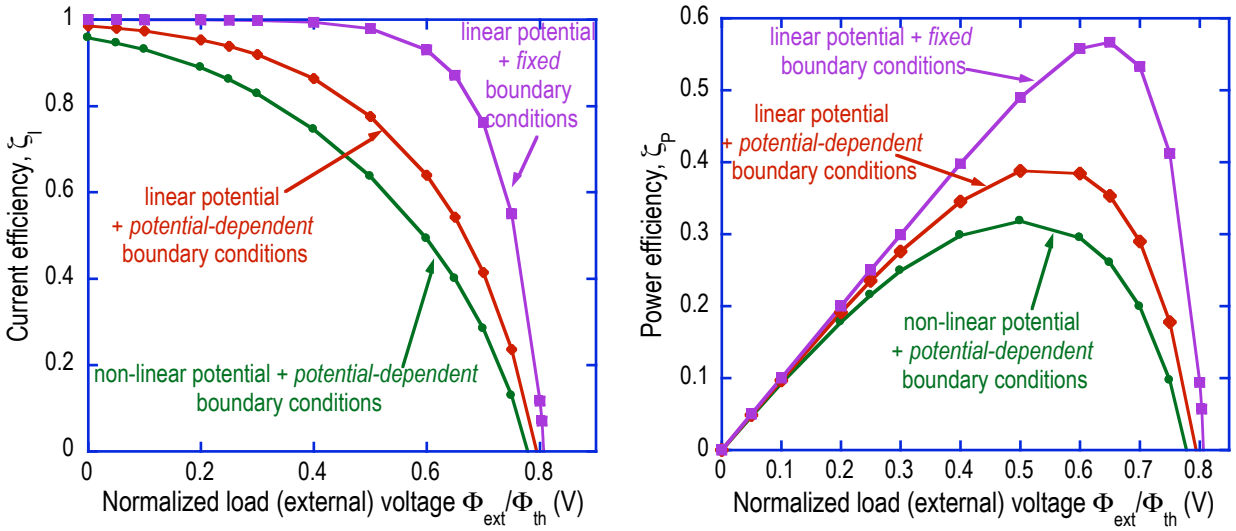

Figure 1. Comparison of the current and power efficiency from various models for an SOFC with an acceptor-doped ceria electrolyte, at 800 °C.

material properties is crucial for the resolution of many macro-issues. Otherwise, the field has to resort to the wasteful, though endemic, "cook and look" approach and/or gross oversimplifications. The latter approach is also popular, but it often leads to exaggerated expectations and erroneous conclusions.

Conversely, developing an accurate model, with minimal assumptions, to describe the dependence of point defect concentration on SOFC operating conditions, allows for a "roots- up" approach to resolving the problems besetting SOFC development. For example, in the failure analysis software developed by the national laboratories and SECA industrial teams, the crude circuit approximations used in the *elements* (or *mesh*) of the numerical models can be replaced by a more appropriate continuum-level electrochemical component that does not force the SOFC to respond ohmically. Moreover, the thermo-elastic properties of the components can be readily incorporated into the failure analysis software.

Present SOFC failure analysis and simulation models used by PNNL and ORNL contain the following modules: (a) electrical power system, (b) thermal system, (c) stack and (d) cell. The latter two modules incorporate continuum-level electrochemical models that describe the fundamental processes that account for the performance of the cell and stack. The current degree of sophistication of the electrochemical models employed, outlined in Ref. 3, uses fixed (i.e., independent of the amount of current delivered by the SOFC) resistances for the electrolyte. Second, anode and cathode effects (ostensibly, their overpotentials), are limited to standard Butler-Volmer treatment without consideration of their interaction with other cell components.

Clearly, a more sophisticated approach would yield more useful results. Accordingly, by extending our earlier work, we have used the continuum-level electrochemical model to describe the effects of operating conditions for SOFC components. Hence, the continuum-level electrochemical model was used to calculate the concentration of defects as a function of P_{O_2}, to predict the performance of SOFCs in steady state and transient conditions, to describe the thermo-mechanical properties of SOFC components, including microstructural effects and to determine the thermo-chemical stability of SOFC components as a function of their thickness ratios and operating conditions of the SOFC. Moreover, the continuum-level electrochemical model was verified through a number of experiments and crucial material constants obtained from said experiments.

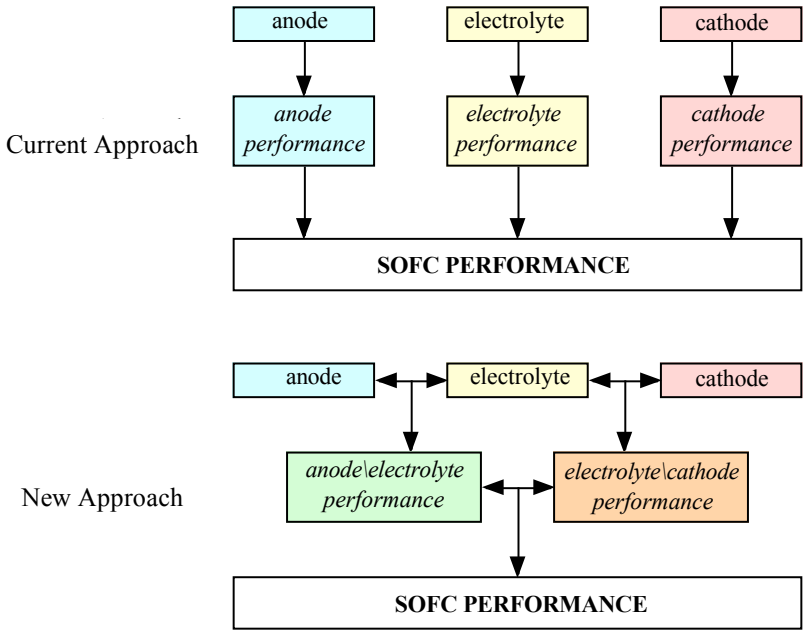

Figure 2. Comparison of conventional and newly developed modeling schemes.

Furthermore, the SOFC performance was not treated as arising from isolated contributions of the components, as depicted by the "current approach" in Fig. 2. This was necessary because, as demonstrated earlier, the components of a multilayer behave co-dependently, as shown in the "new approach" in Fig. 2, and the interaction between the layers is a function of the operating conditions. Thus, the overall objectives of the research project were:

- Advance the fundamental understanding of the continuum-level electrochemistry of oxide mixed ionic-electronic conductors (MIECs) in relation to their performance in SOFCs;
- Extend the models to multilayer structures and incorporate microstructure;
- Obtain, by appropriate experimentation, the fundamental constants required for implementation of model;
- Verify the models through experiment;
- Develop a transient version of the continuum-level electrochemical model;
- Obtain time constants for various transport processes from electrical impedance spectroscopy to examine the effects of transients on SOFC performance;
- Develop and deliver software modules for incorporation of the continuum-level electrochemical model into SOFC failure analysis software used by NETL, PNNL, ORNL and the SECA industrial teams.

EXECUTIVE SUMMARY

Based on the fundamental laws of physics and thermodynamics we developed analytical models to predict the electrochemical performance of SOFCs, and thermo-mechanical and thermo-chemical stability of SOFC materials. These models were derived with minimal approximations (e.g., the defect concentrations in the ceramic lattice were assumed to be within the dilute limit) and due to their fundamental nature provide SOFC developers the necessary tools to select new materials and microstructures and predict their impact on SOFC performance and stability.

The models were developed to relate the concentration of point defects in common SOFC materials with the fluorite structure (YSZ, GDC, and ceria) to environment (oxygen partial pressure and temperature), SOFC operating conditions (load voltage and current in both steady state and transient conditions) for single layer and multilayer architectures.

The models were demonstrated to be self-consistent, in that by obtaining fundamental constants from a single experiment (e.g., equilibrium constant for oxygen-vacancy formation from thermogravimetry) we could use the same constant to model everything from conductivity to thermo-chemical expansion and elastic modulus, without modification or arbitrary fitting parameters. Further, the models and their predictions were experimentally verified to be correct.

The extensive body of work has resulted in 14 publications in scientific journals, ranging from the *Journal of the Electrochemical Society* to *Journal of Applied Physics*. Some of the highlights of this work are:

- A simple analytical expression for the thermo-chemical expansion (both temperature and P_{O_2} effect) for YSZ and GDC was developed and validated. A solution was also obtained and validated for ceria but requires numerical methods to solve due to defect association effects.
- A simple analytical expression for the P_{O_2} effect on bulk elastic modulus was developed and validated for YSZ and GDC. A solution was also obtained and validated for ceria but requires numerical methods to solve due to defect association effects.
- The effect of P_{O_2} on the elastic modulus of polycrystalline YSZ, GDC, and ceria was experimentally demonstrated to be similar to that predicted from our models for the bulk elastic modulus.
- A model was developed to determine the P_{O_2}, and thus chemical stability, between SOFC constitutive layers under operating conditions.
- A complete solution for the electrochemical performance of SOFCs was developed. The model takes into account all the important factors contributing to the electrochemical performance of SOFCs, such as component (anode, electrolyte, cathode) thickness, thickness ratio, microstructure, gas composition, temperature material type and operating conditions (current density, P_{O_2} at the electrodes, overpotential) and does so with less fitting parameters than any other existing model.
- The SOFC electrochemical performance model was extended to transient (both power conditioning and air/fuel disruptions) operation. The model shows the effect SOFC layer

thickness has on the transient time constants and its implications should be considered in SOFC design.

- A technique was developed to improve the quality of Electrochemical Impedance Spectroscopy (EIS) data and applied to de-convolute LSM and LSCF cathode impedance, into their various contributions, while simultaneously obtaining the time constant for each of the relevant processes.
- By analyzing this de-convoluted cathode impedance data and comparing it with quantified cathode microstructure data (from our DOE High Temperature Electrochemistry Center contract # DE-AC05-76RL01830) we were able to, for the first time ever, directly and quantitatively relate cathode polarization to specific microstructural features (triple phase boundary length and pore surface area).
- Finally, software modules for the analytical models were written in the computer languages, C++ and PHP capable of operating on a simple PC or incorporated into CFD (computational fluid dynamics) software used by SECA teams.

The models are directly relevant to SOFC developers both in optimizing their design with existing materials and in considering new materials and architectures to improve their design. While the appropriate materials constants were obtained and the models validated for fluorite based (electrolyte) materials, the models would have even more utility if the materials constants were obtained, and models validated for, perovskite based (cathode) materials. This would then complete the models and materials set necessary for developers to rationally design SOFCs.

EXPERIMENTAL

MODEL DEVELOPMENT

Analytical models were derived from the fundamental laws of physics and thermodynamics with minimal approximations made to describe the potential distribution in the oxide lattice (e.g., the defect concentrations in the ceramic lattice were assumed to be within the dilute limit). The models relate the concentration of point defects to environment (oxygen partial pressure), SOFC operating conditions (load voltage and current in both steady state and transient conditions) for single layer and multilayer architectures. Models were also developed to relate electrical conductivity, thermo-chemical expansion, and elastic modulus to environment (oxygen partial pressure), SOFC operating conditions (load voltage and current in both steady state and transient conditions). Finally, software modules for the analytical models were written in the computer languages, C++ and PHP capable of operating on a simple PC or incorporated into CFD (computational fluid dynamics) software used by SECA teams.

MECHANICAL PROPERTIES: THERMO-CHEMICAL EXPANSION

Sample Preparation

Micron size powders of undoped ceria (Alfa Aesar) and zirconia stabilized with 8mol% yttria (Tosoh Corp.) as well as nanometer size ceria doped with 10 mol% gadolinium (Rhodia) were obtained commercially. Half of the GDC powder was annealed at 1500 °C for 5 hours and then milled in water to increase particle size and improve processability. All the powders were mixed with a polyvinyl butyral (PVB) binder then poured into a cylindrical shaped polyurethane isopress bag (Trexler Rubber Co.) and pressed isostatically to 200MPa. The resulting green bodies were bisqued for binder removal and finally sintered.

The GDC and undoped ceria were sintered at 1600 °C for 5 hours to yield 92% and 90% theoretical densities, respectively. The YSZ was sintered at 1550 °C for 5hrs to yield a density of

99% theoretical. The dense ceramic bodies were then cut lengthwise using a diamond saw and the ends polished parallel to produce samples approximately 25 mm in length and 9 mm in diameter. The samples were then individually tested in the dilatometer.

Measurement of Thermo-Chemical Expansion

Dilatometry was accomplished using a Theta Dilatronic Dilatometer with a fused silica rod, sample holder, and atmosphere enclosure. The temperature profile consisted of heating the samples at a rate of 5 °C/min to 800 °C in air and subsequently isothermally step-changing the ambient P_{O_2} of the sample, allowing long periods of time between steps for equilibration.

The P_{O_2} was controlled by flowing air, argon, and hydrogen as well as mixtures thereof through a temperature controlled water bubbler. The P_{O_2} in the range of $10^{-17} - 10^{-22}$ atm were produced by bubbling mixtures of argon and hydrogen through water at temperatures of up to 40 °C, while heating the gas lines to prevent water condensation. The P_{O_2} was measured using an oxygen sensor, constructed in the lab, consisting of a zirconia tube held at 800 °C, through which the gas to be measured flowed. A platinum conductive coating was applied to a section on either side of the zirconia tube to which platinum wire was attached. The potential generated between the two platinum leads was measured and corresponded to the P_{O_2} of the mixture via the Nernst equation. The measured P_{O_2} values at very low P_{O_2} were no more than an order of magnitude greater than that calculated based on the feed gas composition, the difference probably due to very small gas leaks in the apparatus.

Characterization Techniques

The crystal structure and the texture of the samples were studied using X-Ray diffraction (XRD) with Cu K_α radiation (Philips APD 3720). The density of as-sintered ceria samples were measured by the immersion technique (i.e., Archimedes Principle). Optical and Scanning Electron Microscopy (SEM, JEOL JSM 6400) were employed for microstructural characterization.

MECHANICAL PROPERTIES: ELASTIC MODULUS AND FRACTURE TOUGHNESS

Sample Preparation and Heat Treatments

Pure ceria powder was mixed with 3 wt% polyvinyl butyral (PVB) ethanol solution by ball milling for 24 hours. After drying, ceria samples were prepared by uniaxial pressing followed by cold isostatic pressing at 250 MPa for 5 minutes. The samples were held at 400 °C for one hour and then sintered at 1550 °C for 20 hours with a heating and cooling rate of 5 °C/min. The final size of the ceria samples was about Φ 6 mm × 4 mm. The strength of pure ceria was measured using bending test samples with dimensions of 2.6 mm × 4 mm × 45 mm. The fracture toughness of pure ceria was measured using Brazilian disk samples with the dimensions of Φ 26 mm × 2.6 mm. The GDC and YSZ samples for nano-indentation tests were pressed and sintered similar to the ceria samples but their final size was Φ 10 mm × 4 mm.

Prior to heat treatment, all samples for nano-indentation tests were carefully polished down to 0.25 μm using alumina powder. For pure ceria, the Brazilian disk samples were polished down to 600 grit using silicon carbide sand paper. The surface finish of bending bar samples was machined according to ASTM C1161 standard.

To create different defect concentrations, the as-sintered samples were heat treated in a tube furnace at 800 °C under different P_{O_2} using air, N_2, H_2, and H_2/H_2O gases for 15 hours until equilibrium was reached at a depth larger than 1.3 mm for ceria and GDC and larger than 0.6 mm for YSZ, based on equilibrium distance calculations[3] using the oxygen self-diffusivity coefficients given by B.C.H. Steele[4] and P.S. Manning[5]. The P_{O_2} was measured using a zirconia oxygen sensor connected to the out-gassing line of the furnace. Samples were then fast cooled to room temperature to maintain the oxygen vacancy concentration achieved at the elevated temperature. The average cooling rate was about 16 °C/min for the first 200 °C, 9 °C/min for the range from 600 °C–400 °C. The total time for the samples to cool down to 300 °C was about 50 minutes. In order to distinguish between the thermal vacancies and those created by a reduced atmosphere, one sample of each material was heat treated in air (P_{O_2} = 0.21 atm) for the same amount of time at 800 °C and then fast-cooled to room temperature. To prevent re-oxidizing during cooling, the gas mixture flowed continually during the fast-cooling period.

After heat treatment, the ceria and GDC samples became noticeably darker as the applied P_{O_2} decreased, which is an indication that the vacancy concentrations were conserved. The color change on the surface was strongest immediately after the heat treatment. However, it decayed somewhat over time, even at room temperature. The color fading rate for GDC was very fast and took only several hours for the surface color to change from black (after H_2 reduction) to a light brownish color. However, the process was very sluggish in the pure ceria samples. For YSZ samples, the color did not change noticeably even under very low P_{O_2}, which suggests that the defect concentration was not increased significantly upon heat treatment. It should be noted that the re-oxidation in air for all three materials was limited only to a very thin layer on the surface owing to the low diffusion rates at room temperature.

Mechanical Testing

The intrinsic elastic modulus was measured using nano-indentation test technique at room temperature. Preliminary nano-indentation results conducted on the surface of the as heat treated samples showed a large scatter in data. Further analysis using SEM revealed the etching of the surface upon heat treatment. Therefore, the samples were mechanically polished after heat treatment and prior to nano-indentation in order to remove the top layers (< 10 μm) altered by the thermal etching and by the aforementioned re-oxidization.

The nano-indentation was carried out using Hysitron Tribo-Indenter. The samples were loaded to 5000 μN and held for 5 seconds and then unloaded. The loading and unloading rates were the same and equal to 1000 μN/s. The reduced modulus (E_r) was calculated from the slope of the unloading segment of the load-displacement curve. This reduced elastic modulus combines the modulus of the indenter and the specimen according to Eq. (4).

$$\frac{1}{E_r} = \frac{(1-\upsilon^2_{indenter})}{E_{indenter}} + \frac{(1-\upsilon^2_{sample})}{E_{sample}} \tag{4}$$

Where, $\upsilon_{indenter}$ and υ_{sample} are the poisson ratios and $E_{indenter}$ and E_{sample} are the elastic modulus of the diamond indenter and the sample, respectively. The elastic modulus of the

sample was calculated using $\upsilon_{indenter}$=0.07 and $E_{indenter}$=1140 GPa for the diamond indenter and assuming υ_{sample}= 0.3.

For the purpose of comparison with the nano-indentation results, the elastic modulus of bulk samples by four-point-bending was also conducted at room temperature. Prior to heat treatment, the bending bar samples were sent to be machined (PremaTech Advanced Ceramics, USA) according to the ASTM C 1161 standard. The bulk elastic modulus was measured using an MTS810 mechanical testing system designed for controlling small displacements. The displacement was measured using MTS model 632.06B-20 extensometer at 0.016 inch full scale range. The load was measured using MTS 661.19-2200 lbs load cell at 200 lbs full scale range. The support span of the bending fixture was 30 mm, and a one-third loading span was used.

The loading speed was calculated according to ASTM D 6272 as

$$R = \frac{0.185ZL^2}{d} \tag{5}$$

where, R is the displacement rate; L is the support span (30 mm), d is the depth of the beam (2.6 mm); Z is the strain rate of the outer potion of the sample and is equal to 0.01 s^{-1}. Therefore, the displacement rate was then determined to be 0.6 mm/min. A computer (LabView 7, National Instruments software) was used for the data acquisition.

The elastic modulus was calculated from

$$E_B = \frac{0.21L^3m}{bd^3} \tag{6}$$

where, E_B is the modulus of elasticity in bending; m is the slope of the loading segment of load-displacement curve; b is the width of the bending bar. At least two samples for each heat treatment condition were tested for the bulk elastic modulus.

The flexural strength for pure ceria was also measured by four point bending test. The flexural strength can be expressed as Eq. (7).

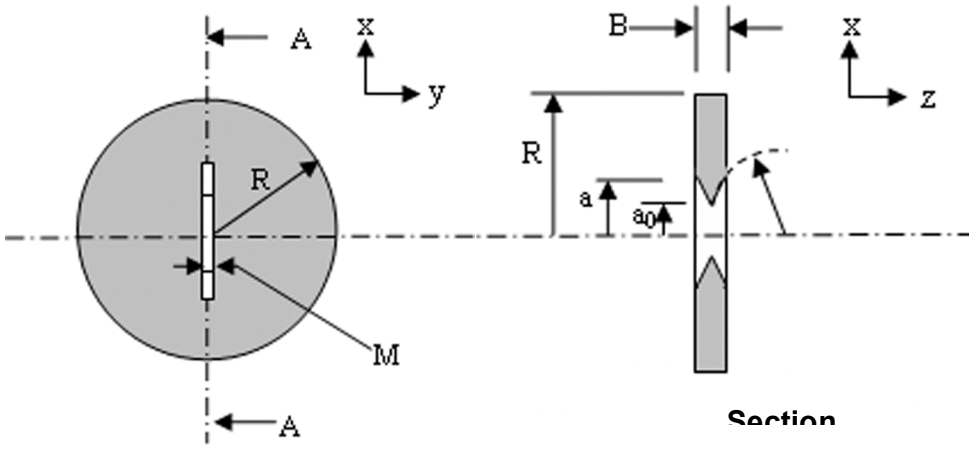

Figure 3. The geometry of the chevron-notched Brazilian disk samples used in the fracture toughness test. The main crack propagation direction is defined as x-direction and the crack opening direction is y-direction. The fracture surface lies on x-z plane.

$$\sigma_f = \frac{PL}{bd^2} \tag{7}$$

where, P is the load at the moment of break, L is the support span, d is the thickness of the testing sample and b is the width of the sample.

The geometry of the Brazilian disk samples used for fracture toughness testing of pure ceria is presented in Fig. 3. Chevron notches were cut in the Brazilian disk samples prior to their heat treatment using a low speed diamond saw with a 0.2 mm-thick blade. The radius of the blade was R_0=12.7 mm. The final dimensions of a typical sample were R=13.03 mm, B=2.62 mm, a_o=3.67 mm, a=6.45 mm, M=0.24mm. The testing method for the K_{13C} measurement followed the procedure explained in the references[6,7]. The loading and unloading of the fracture test was under displacement control mode with a cross head speed of 0.05 mm/min using Instron 1125. The heat treated samples were first pre-cracked by loading under mode I (i.e., by loading in compression along a diameter through the chevron notch) to about 90~95% of the fracture load. The sample was held at this load level for 6~12 minutes and then unloaded. Crack propagation within the Chevron notch is stable because the effective thickness is increased continuously owing to the shape of the notch.

The stress-intensity factors for mode I loading of Brazilian disk samples were calculated using the solutions given by Atkinson, *et. al.*[8] as

$$K_{IC} = \frac{P_c a^{1/2}}{\pi^{1/2} RB} N_1 \tag{8}$$

where P_c is the fracture load, a is the half crack length, and N_1 is a non-dimensional coefficient that is a function of the relative crack size (a/R). Atkinson, *et. al.*[8] gave the numerical solutions for the cracks in the size range (a/R)=0.1-0.6, which were used in this study for calculating K_{1C}.

Characterization Techniques

The crystal structure and the texture of the samples were studied using X-Ray diffraction (XRD) with Cu K_α radiation (Philips APD 3720). The density of as-sintered ceria samples were measured by the immersion technique (i.e., Archimedes Principle). Optical and Scanning Electron Microscopy (SEM, JEOL JSM 6400) were employed for microstructural characterization.

DETERMINATION OF ELECTROCHEMICAL PERFORMANCE-PROPERTY-PROCESSING RELATIONSHIPS

Sample Preparation and Electrochemical Characterization

Symmetrical cathode/YSZ/cathode test samples were produced for the work. The cathodes focused on were LSM ($La_{0.8}Sr_{0.2}MnO_{3-\delta}$) and LSCF ($La_{0.8}Sr_{0.2}Co_{0.2}Fe_{0.8}O_{3-\delta}$). The electrolyte used in the work was prepared by a tape cast method by Marketech International, Inc. The YSZ contained 8 mol % yttria and had dimensions of 10.0 × 20.0 × 0.1 mm. Nextech Materials, Ltd provided the cathode materials. The cathode was screen printed on both sides of the electrolyte in two layers with a square area of 64 mm^2, resulting in a symmetric sample. A drying step was performed after the screen-printing of each layer in a Fisher Isotemp drying oven at 120 °C for one hour. After drying, the resulting test samples were sintered at various temperatures ranging from 1150 to 1325 °C to produce a variety of cathode microstructures. The resulting symmetrical samples had a cathode thickness of about 20 microns and YSZ thickness of 100 microns. The samples were mounted in a quartz reaction tube inside a Barnstead/Thermolyne furnace with pressure contact leads to the frequency response analyzer. The quartz tube consisted of an inlet and outlet for gas flow, gold leads shielded by alumina rods with platinum paint, and a pressure contact sample holder. The gold leads were connected by platinum wires to a platinum mesh, which was used as the current collector. The pressure contact holder was designed in a way that exposes the platinum mesh and adjacent cathode to the ambient gas. Oxygen, air, and argon gases were flowed over the samples in measurement conditions. For oxygen partial pressures at or above 0.01 atm, mass flow controllers were used to regulate the flow of argon and air onto the sample, producing gas flows of known composition at 40 cc/min. For oxygen partial pressures of 0.001 atm and less, a ZIROX SGM5-EL electrolysis device was used to generate the desired concentration at a flow rate of 100 cc/min. Electrochemical Impedance Spectroscopy (EIS) was performed using a Solartron 1260 impedance gain analyzer to measure the frequency response of the prepared samples. Auto-integration was used under “I, long” measurement conditions with an integration time of 60

seconds. I, long is a Zplot option in which the current is measured for noise and an attempt is made to get consistency in the measurements with a maximum standard deviation of 1 % when possible. The active frequency range was 0.01 Hz - 32 MHz. SMART, Zplot™ and Zview™ were used to acquire and display the impedance data.

Microstructural Characterization

Qualitative characterization of the electrode microstructure was performed through Scanning Electron Microscopy (SEM, JEOL JSM 6400). Quantitative analysis was subsequently performed using a dual beam FIB/SEM (FEI Strata DB 235) under support from the Department of Energy High Temperature Electrochemistry Center (DOE-HiTEC) at the University of Florida (Contract #: DE-ACO5-76RL01830). The FIB/SEM was used to create three-dimensional image of the microstructures of the symmetric samples. The dual beam FIB/SEM ablated successive layers with SEM imaging after each ablation. Serial milling in the z-direction was conducted with steps of about 20-50 nm per slice using a Ga^{+} ion beam. After each FIB slice, SEM imaging was performed at a magnification of 12,000X. These uniformly spaced 2-D images were then aligned, producing a 3-D image. The SEM images were then used to calculate the microstructural quantities of interest. Key areas of interest were triple phase boundary length (L_{TPB}), pore surface area, tortuosity, and porosity. Both sets of results were correlated to give an objective relationship between electrochemical performance and cathode microstructure.

RESULTS AND DISCUSSION

CONTINUUM-LEVEL ELECTROCHEMICAL MODEL

In Phase I of the project a unified framework for understanding the effects of point defects on the mechanical, chemical, and electrical properties of ceramic materials was developed, resulting in a continuum-level electrochemical model. Preliminary experimental results from Phase I indicated we were on the correct track, and in Phase II of the project the model was extended to multilayer structures, chemical stability and transient response and fully validated. The model development and ensuing validation are described below.

Dependence of Defect Concentration on P_{O_2}

Using the familiar Kröger-Vink notation[9], the defect equations governing fluorite-structured oxides, like ceria, are given below. A dilute solution is assumed so the activity of the host lattice is unity. All the *K*'s are equilibrium (mass action) constants for the immediately preceding reactions, *c* is concentration and subscripts *e*, *h*, *v* and *i* refer to electrons (e'), holes ($h^{\bullet}$), oxygen vacancies ($V_O^{\bullet\bullet}$) and oxygen interstitials (O_i''), respectively.

Electron-Hole Pair Formation. Thermal generation of electron-hole pairs (e', $h^{\bullet}$) is given by:

$$null \leftrightarrow e' + h^{\bullet} \qquad K_t = c_e c_h \tag{9}$$

External Equilibria. Equilibrium between the oxide sublattice ($O_O^{\times}$) and the gas phase (O_2) occurs by exchange of oxygen between the crystal lattice and the gas as follows

$$O_O^{\times} \leftrightarrow V_O^{\bullet\bullet} + 2e' + \tfrac{1}{2}O_2 \qquad K_r = c_v c_e^2 P_{O_2}^{\frac{1}{2}} \tag{10a}$$

We note here that the electronic species formed by the reactions in Eqs. (9) and (10) are *typically* localized on the metal cation, M, of the fluorite:

$$\mathrm{M}_{\mathrm{M}}^{\times} + e' \leftrightarrow \mathrm{M}_{\mathrm{M}}' \tag{10b}$$

Internal Disorder. Anti-Frenkel disorder is the primary type of internal disorder found in fluorites and is given by

$$\mathrm{O}_{\mathrm{O}}^{\times} \leftrightarrow \mathrm{V}_{\mathrm{O}}^{\bullet\bullet} + \mathrm{O}_{\mathrm{i}}'' \qquad K_f = c_v c_i \tag{11}$$

Doping. Because it predominates in technically useful oxide ceramics, we consider only fixed-valence-acceptor doping, where the dopant concentration, c_a, is constant. For example

$$\mathrm{A_2O_3} \xrightarrow{\mathrm{MO_2}} 2\mathrm{A}_{\mathrm{M}}' + \mathrm{V}_{\mathrm{O}}^{\bullet\bullet} + 3\mathrm{O}_{\mathrm{O}}^{\times} \tag{12}$$

Charge Balance. Since the material is electrically neutral,

$$c_e + c_a + 2c_i = 2c_v + c_h \tag{13}$$

As discussed earlier, to understand the effect of point defects on various physical properties of ceramics, it is helpful to first obtain analytical equations for the defect concentration dependence on $P_{\mathrm{O_2}}$. We will now develop such a model for fluorite structured oxides, with acceptor-doped ceria as out case study, in a *region of interest* (i.e., where the material is usually employed).

Acceptor-doped ceria and many other ceramics are used in $P_{\mathrm{O_2}} \leq 0.21$ atm, which is defined, therefore, as our *region of interest*. In the *region of interest*, $c_a >> c_i$ and $c_v >> c_h$ [6], so the charge balance becomes,

$$c_e + c_a = 2c_v \tag{14}$$

Hence, combining Eqs. (10) and (14) yields:

$$K_r^{\frac{1}{2}} c_v^{-\frac{1}{2}} P_{O_2}^{-\frac{1}{4}} + c_a = 2c_v \tag{15}$$

which, when differentiated with respect to c_v ($dK_r/dc_v = 0$ since K_r is a function of temperature only; the assumption here is that the energy expended in creating a vacancy is independent of the number of vacancies created previously), gives:

$$-\frac{dP_{O_2}}{dc_v} = 8K_r^{-\frac{1}{2}} c_v^{\frac{1}{2}} P_{O_2}^{\frac{5}{4}} + 2P_{O_2} c_v^{-1} \tag{16}$$

For $P_{O_2} >> 4^{-4} K_r^2 c_v^{-6}$, Eq. (16) reduces to:

$$-\frac{dP_{O_2}}{dc_v} \approx 8K_r^{-\frac{1}{2}} c_v^{\frac{1}{2}} P_{O_2}^{\frac{5}{4}} \tag{17}$$

This constraint is satisfied for P_{O_2}'s in the *region of interest* where $2c_v \geq c_a$ ($c_a \sim 10^{27}$ m^{-3}).

From Eqs. (10) and (14), as $P_{O_2} \rightarrow \infty$ (i.e., at the upper limit of the *region of interest*), $2c_v \rightarrow c_a$ (and $c_e \rightarrow 0$). Eq. (17) may then be solved by integration, as shown below

$$K_r^{\frac{1}{2}} \int_{\infty}^{P_{O_2}} P_{O_2}^{-\frac{5}{4}} \cdot dP_{O_2} = -8 \int_{\frac{1}{2}c_a}^{c_v} c_v^{\frac{1}{2}} \cdot dc_v$$

with the result

$$c_v = \left[\tfrac{3}{4} K_r^{\frac{1}{2}} P_{O_2}^{-\frac{1}{4}} + \left(\tfrac{1}{2} c_a \right)^{\frac{3}{2}} \right]^{\frac{2}{3}} \tag{18}$$

In addition, combining Eq. (18) and Eq. (10) yields:

$$c_e = K_r^{\frac{1}{2}} P_{O_2}^{-\frac{1}{4}} \left[\tfrac{3}{4} K_r^{\frac{1}{2}} P_{O_2}^{-\frac{1}{4}} + \left(\tfrac{1}{2} c_a \right)^{\frac{3}{2}} \right]^{-\frac{1}{3}} \tag{19}$$

Unlike expressions derived using the Brouwer approach[10], Eqs. (18) and (19) are continuous throughout the *region of interest*.

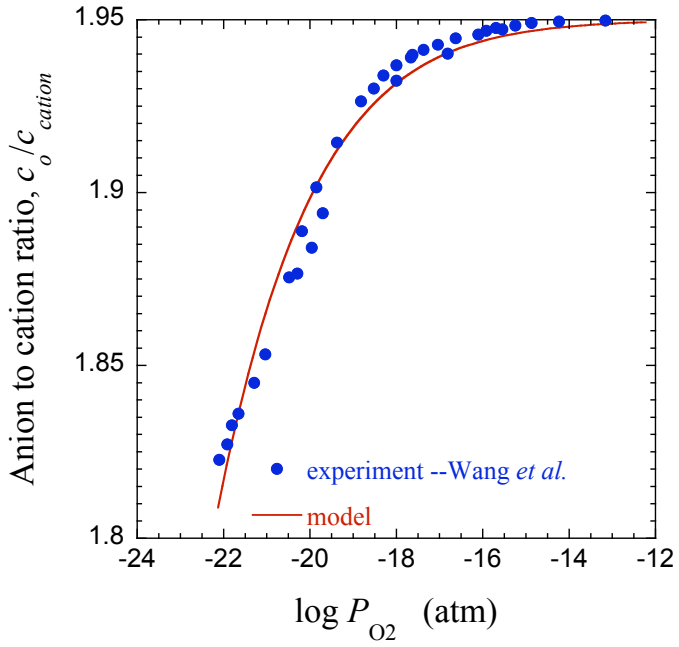

Figure 4. Dependence of c_o/c_{cation} atom ration on oxygen partial pressure for GDC; (●) themogravimetric data from Wang *et al.*[11], (−) model.

To obtain a reasonable value for K_r, Eq. (18) was rewritten as

$$\frac{c_o}{c_{cation}} = 2 - \frac{1}{c_{cation}}\left[\tfrac{3}{4}K_r^{\frac{1}{2}}P_{O_2}^{-\frac{1}{4}} + \left(\tfrac{1}{2}c_a\right)^{\frac{3}{2}}\right]^{\frac{2}{3}} \qquad \text{since} \quad c_v + c_o = 2c_{cation} \qquad (20)$$

where c_{cation} is cation concentration and c_o is oxygen ion concentration. Eq. (20) was then fitted to data from Wang *et al.*[11] who used thermogravimetry to obtain the non-stoichiometry of $Ce_{0.9}Gd_{0.1}O_{1.95-\delta}$ (GDC) as a function of P_{O_2}. Using $c_a \approx 1.25$ nm^{-3},[12,13] a good fit to the data was obtained in Fig. 4 for $K_r = 1.3 \times 10^{-9}$ atm$^{1/2}$nm^{-9}. This compares quite favorably with results reported by Tuller and Nowick[14] (4×10^{-11} atm$^{1/2}$nm^{-9} for $CeO_{2-\delta}$) and Otake *et al.*[15] (6×10^{-11} atm$^{1/2}$nm^{-9} for $Ce_{0.9}Y_{0.1}O_{1.95-\delta}$). However, as Otake *et al.* show, these values are dependent on the defect model used to extract them from experimental data.

Equations (18) and (19) are plotted in Fig. 5, for acceptor-doped ceria, along with results from the Brouwer approach[10] and a numerical solution that has no simplifying assumptions. The close agreement of our results with the numerical solution demonstrates the validity and accuracy of the model in describing the defect equilibria of the aforementioned defect species in

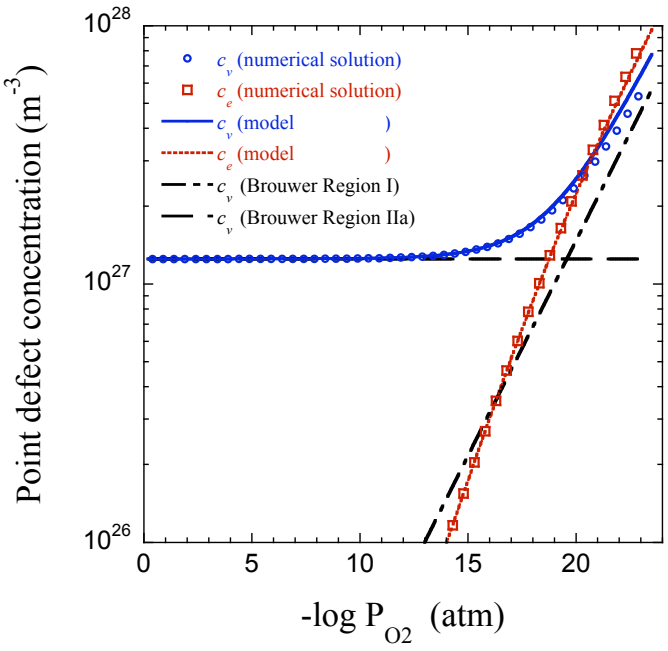

Figure 5. Comparison of defect concentration as a function of P_{O_2} (using $c_a \approx 1.25$ nm^{-3} [12,13] and $K_r = 1.3 \times 10^{-9}$ atm$^{1/2}$nm^{-9}) obtained from numerical solution of the defect equations (open symbols); from Eqs. (11) and (12); and from the Brouwer approach[10].

the *region of interest*. Moreover, unlike expressions derived using the Brouwer approach[10], Eqs. (18) and (19) are continuous in the *region of interest*.

Having modeled the dependence of defect concentration on operating conditions (i.e., P_{O_2}), we turn our attention to some of the pertinent physical properties of ceramics and model their dependence on defect concentration.

Extension of Continuum-Level Electrochemical Model to Electrical Conductivity

The electrical conductivity of a ceramic typically has both ionic and electronic contributions. For GDC, (in the *region of interest*) oxygen vacancies and electrons are the charge carriers and so (incorporating Eqs. (18), (19)) the electrical conductivity is given by:

$$\sigma_{tot} = z_v q u_v c_v + z_e q u_e c_e = z_V q u_V \left[\tfrac{3}{4}K_r^{\frac{1}{2}}P_{O_2}^{-\frac{1}{4}} + \left(\tfrac{1}{2}c_a\right)^{\frac{3}{2}}\right]^{\frac{2}{3}} + z_e q u_e K_r^{\frac{1}{2}}P_{O_2}^{-\frac{1}{4}}\left[\tfrac{3}{4}K_r^{\frac{1}{2}}P_{O_2}^{-\frac{1}{4}} + \left(\tfrac{1}{2}c_a\right)^{\frac{3}{2}}\right]^{-\frac{1}{3}} \qquad (21)$$

where z is the charge on the point defect, q is the elementary electronic charge and u is electrical

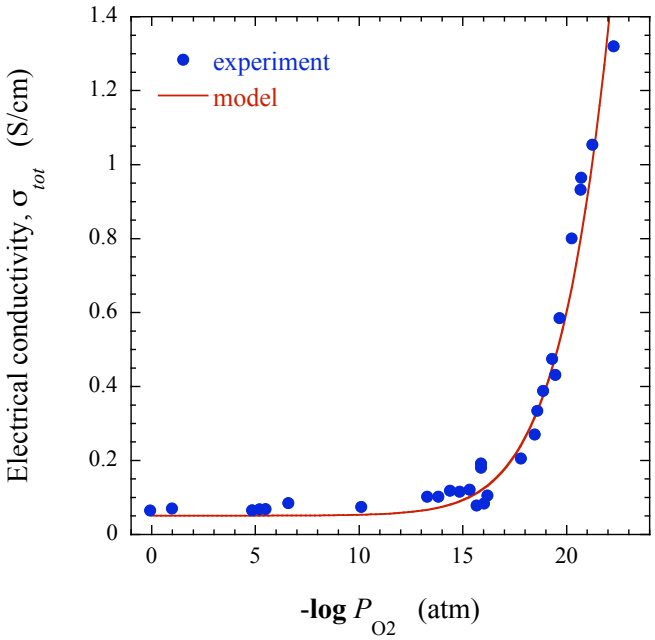

Figure 6. Electrical conductivity dependence on P_{O2} for GDC; (●) data from Wang *et al.*[16], (−) model.

mobility. We hasten to point out that we are certainly not the first to derive conductivity dependence on P_{O_2} for oxides. However, as discussed earlier, previous models rely on relationships derived from the Brouwer approach[10], which are discontinuous across Brouwer regimes. The novelty of the model developed herein is that it provides continuous equations for the point defect concentration on P_{O_2} in the region of interest, which, for acceptor-doped ceria (our case study), spans two Brouwer regimes. Accordingly, physical properties modeled using this relationship will also be continuous in the same range.

Figure 6 shows a plot of Eq. (21) fitted to conductivity data from Wang *et al.*[16] for GDC. The excellent fit to the conductivity data demonstrates the accuracy of the model in predicting the effect of point defect concentration on electrical conductivity. The good fit was obtained using the same K_r value obtained from fitting GDC non-stoichiometry (Fig. 4) and $u_V \approx 1.3\times10^{-8}$ $V^{-1}m^2s^{-1}$ as reported by Steele[17]. The electron mobility, u_e, was then adjusted to obtain the best fit to the data, which corresponds to $u_e = -1.45\times10^{-3}$ $V^{-1}cm^2s^{-1}$. This value for u_e is a bit lower than other reported values[17,18] , and this is most likely because GDC was not constricted to a single Brouwer regime. It is easy to see that limiting GDC to the *electrolytic* regime ($\sigma_e = 2^{\frac{1}{2}} z_e q c_a^{-\frac{1}{2}} K_r^{\frac{1}{2}} \cdot u_e \cdot P_{O_2}^{-\frac{1}{4}}$)[19] will yield higher u_e values, while limiting GDC to the *highly*

reducing regime ($\sigma_e = 2^{\frac{1}{3}} z_e q K_r^{\frac{1}{3}} \cdot u_e \cdot P_{O_2}^{-\frac{1}{6}}$)[19] will give lower u_e values for any given σ_e. Typically, the former is assumed in the literature[17,18].

Extension of Continuum-Level Electrochemical Model to Defect Transport

We have developed a complete solution for the electrochemical performance of SOFCs in both steady state and transient conditions. The model takes into account all the important factors contributing to the electrochemical performance of SOFCs, such as component (anode, electrolyte, cathode) thickness, thickness ratio, microstructure, gas composition, temperature material type and operating conditions (current density, P_{O_2} at the electrodes, overpotential).

Steady State. In steady state conditions, the solution for oxygen vacancy concentration and flux density, for *n*-type oxide MIECs, is as follows[20,21]

$$c_v(x) - c_{v,0} + \frac{c_a}{(z_v - z_e)}\left(\frac{J_v + \beta J_e}{J_v - z_v \beta J_e}\right) \cdot \mathbf{ln}\left(\frac{c_v(x) - \frac{J_v c_a / z_v}{J_v - z_v \beta J_e}}{c_{v,0} - \frac{J_v c_a / z_v}{J_v - z_v \beta J_e}}\right) = -\frac{(J_v - z_v \beta J_e)}{z_v (z_v - z_e) q D_v} x \qquad (22a)$$

$$\phi(x) = \phi_0 - \frac{\lambda c_a}{(z_v - z_e)}\left(\frac{J_v + \beta J_e}{J_v - z_v \beta J_e}\right) \cdot \mathbf{ln}\left(\frac{c_v(x) - \frac{J_v c_a / z_v}{J_v - z_v \beta J_e}}{c_{v,0} - \frac{J_v c_a / z_v}{J_v - z_v \beta J_e}}\right) \qquad (22b)$$

$$\gamma = \frac{J_v - z_v \beta J_e}{z_v (z_v - z_e) q D_v} = \frac{\phi_L - \phi_0}{\lambda L} - \frac{c_L - c_0}{L} \qquad (22c)$$

$$J = J_{ex}\left[\mathbf{exp}\left(\alpha \frac{q}{k_B T} \eta_{act}\right) - \mathbf{exp}\left(-(1-\alpha)\frac{q}{k_B T}\eta_{act}\right)\right] \qquad (22d)$$

$$P_{O_2,\text{cathode-electrolyte interface}} = P_{\text{atmos}} - \left(P_{\text{atmos}} - P_{O_2 @ \text{air}}\right)\mathbf{exp}\left(\frac{kT}{4q} \cdot \frac{\tau_c}{D_c} \cdot \frac{L_c}{\varepsilon_c} \cdot J\right) \qquad (22e)$$

$$P_{\mathrm{H_2,anode\text{-}electrolyte\ interface}} = P_{\mathrm{H_2}@\mathrm{fuel}} - \frac{kT}{2q}\cdot\frac{\tau_a}{D_a}\cdot\frac{L_a}{\varepsilon_a}\cdot J \tag{22f}$$

$$P_{\mathrm{H_2O,anode\text{-}electrolyte\ interface}} = P_{\mathrm{H_2O@fuel}} + \frac{kT}{2q}\cdot\frac{\tau_a}{D_a}\cdot\frac{L_a}{\varepsilon_a}\cdot J \tag{22g}$$

where $\lambda = (z_V - z_e)k_BT/(z_eqc_A)$, $\beta = D_v/D_e$, z is charge equivalence, q is the elementary electronic charge, J_{ex} is the exchange current density, α is the apparent charge transfer coefficient, J is total current density, J_V is oxygen vacancy current density, J_e is electronic current density, L is electrolyte thickness, , ϕ is the Galvani potential, k is Boltzmann's constant, T is temperature, L_a is anode thickness, L_c is cathode thickness, ε_a is anode porosity, ε_c is cathode porosity, D_V is oxygen vacancy diffusivity, D_e is electron diffusivity, D_a is gas diffusivity through the anode, D_c is gas diffusivity through the cathode and γ is a constant obtained from the boundary conditions, τ_c is cathode tortuosity, τ_a is anode tortuosity and P is partial pressure. The subscripts 0 and L refer to the boundary values of the MIEC, i.e., at $x = 0$ (anode side) and $x = L$ (cathode side).

Previous researchers[22,23,24] used *fixed* boundary values for the defect concentrations and linear potential distributions. *Fixed* boundary values are independent of the load voltage, Φ_{ext}. This implies that Φ_{ext} only affects the spatial distribution of defects inside the MIEC. In principle, this is not possible, since the activities of *all* the reacting chemical species cannot be held constant while changing the potential at the interface [25,26]. *Potential-dependent* boundary conditions were obtained by including the effect of the load voltage on the boundary values of the defect concentrations. Our results, exemplified in Eq. (22), allow for the prediction of transport properties of the MIEC components and SOFC performance. Moreover they show that using fixed boundary conditions and assuming a linear Galvani potential leads to an overestimation of cell performance. Assuming a linear potential ignores the efficiency sapping effects of mixed conduction and using *fixed* (i.e., independent of potential) boundary concentrations lessens the effects of changing concentration gradients. Consequently, when these assumptions are removed the projected cell performance is reduced. This demonstrates the importance of using the best available electrochemical models in the computation of overall SOFC performance.

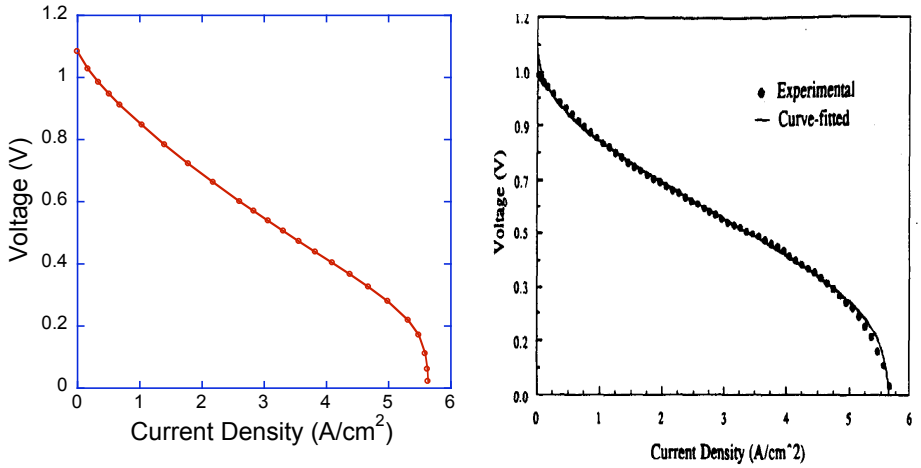

Figure 7. Comparison of theoretical models fit to experimental data for anode-supported Ni-YSZ/YSZ/LSM-YSZ SOFC operated at 800 °C with H_2 bubbled through water (at 33 °C) at the anode and air at the cathode: (a) present work (b) Kim *et al*[27].

Figure 7 shows a comparison of our results compared with that of Kim, Virkar, Fung, Mehta and Singhal [27] for modeling the I-V characteristics of a Ni-YSZ/YSZ/LSM cell. We were able to model cell performance with similar accuracy to Kim *et al*. However, less fitting parameters (three vs. ten) were used in our model to obtain the same fit—we used J_{ex} (the exchange current density), τ_a/D_a (the effective tortuosity of the anode) and τ_c/D_c (the effective tortuosity of the cathode). Moreover, because the continuum electrochemical model does not assume a uniform vacancy concentration it is amenable for modeling cells with mixed conducting electrolytes, e.g., GDC.

Accordingly, Fig. 8 shows a comparison of predicted I-V curve for anode-supported Ni-YSZ/YSZ/LSM-YSZ SOFC and Ni-YSZ/GDC/LSM-YSZ SOFC operated at 800 °C with H_2/H_2O at the anode and air at the cathode. In Fig. 8, both plots were generated with the effective tortuosity of the anode equal to the effective tortuosity of the cathode, i.e., $\tau_a/D_a = \tau_c/D_c = 10^4$ s/m^2 and an exchange current density of 0.1 A/cm^2. The model accurately predicts, consistent with experiments, the lower current density (and power density) achieved with a GDC electrolyte for a given cell voltage—even though GDC has a higher conductivity than YSZ—due to mixed conduction (electronic leakage current) in GDC.

Figure 9 shows the effect of reducing the effective tortuosity which could be achieved by either modifying the electrode microstructure to produce a less tortuous electrode or by using gasses with higher diffusivity gases. Reducing the effective tortuosity results in a dramatic

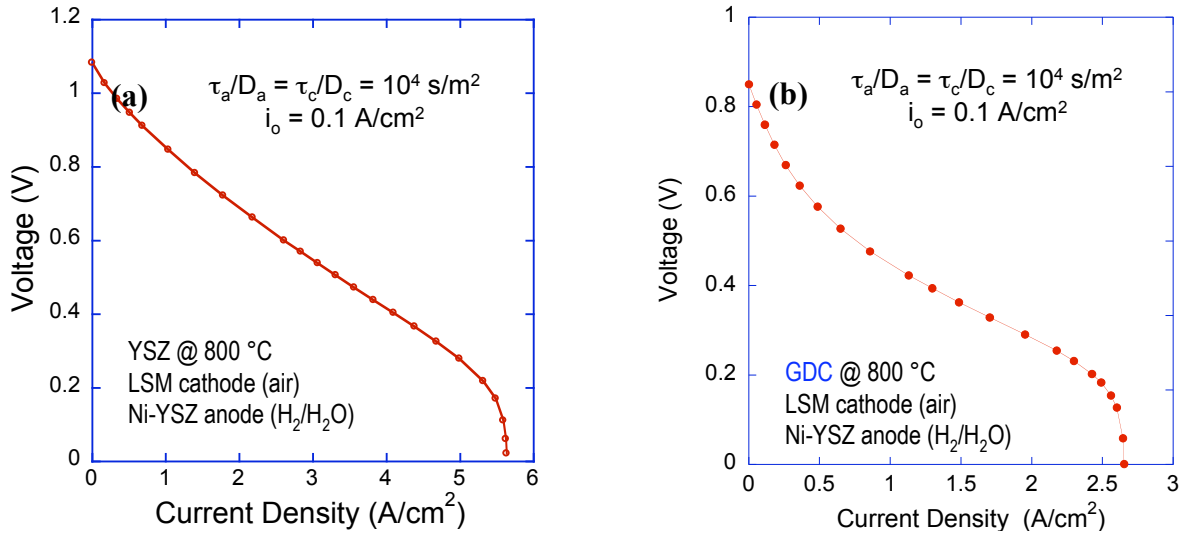

Figure 8. Theoretical I-V curve for anode-supported (a) Ni-YSZ/**YSZ**/LSM-YSZ SOFC and (b) Ni-YSZ/**GDC**/LSM-YSZ SOFC operated at 800 °C with H_2/H_2O at the anode and air at the cathode.

reduction in the concentration overpotential and, accordingly, a factor of three increase in power density. This clearly demonstrates the importance of the electrode microstructure.

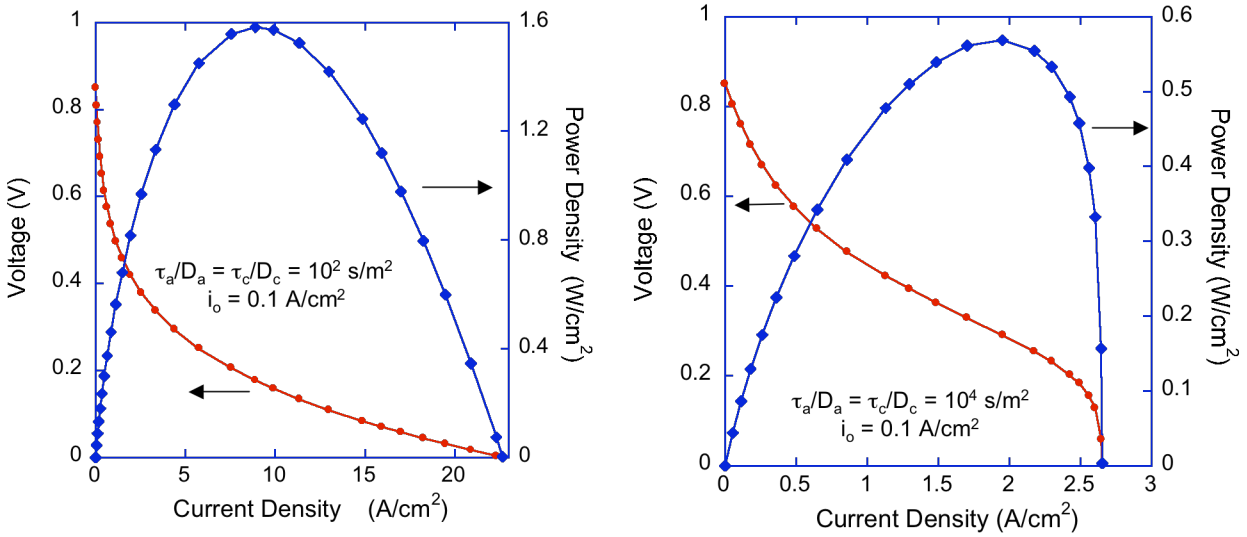

Figure 9. Comparison of theoretical I-V and power density curves for anode-supported Ni-YSZ/GDC/LSM-YSZ SOFC operated at 800 °C with H_2/H_2O at the anode and air at the cathode: (a) effective tortuosity $\tau/D = 10^2$ s/m^2 and (b) $\tau/D = 10^4$ s/m^2.

Transient Response. The continuum-level electrochemical model was extended to transient conditions (more detail may be obtained from the Phase 1 topical report of this project). To obtain solutions, we assumed a linear potential distribution. This assumption is best applied to predominantly ionic conductors, e.g., YSZ or predominantly electronic conductors, e.g., LSM. Two limiting cases are given below. The results of the model gives defect concentration (c) and potential (ϕ) as a function of a 1-D spatial variable (x) and time (t).

Case (1). First, consider the response of the SOFC when it is first placed into a P_{O_2} gradient without a load (i.e., *open-circuit*, $J = 0$). In such conditions $c_e(x = 0, t = 0) = c_e(x = L, t = 0) = c_e^0$, and

$$c_e(x,t) = e^{-\alpha^2\gamma^2 t}\left[\frac{\left(c_e^0 - c_{e,L}^\infty\right) - \left(c_e^0 - c_{e,0}^\infty\right)\cos\gamma L}{\sin\gamma L}\sin\gamma x + \left(c_e^0 - c_{e,0}^\infty\right)\cos\gamma x\right] + \frac{\left(c_{e,L}^\infty - c_{e,0}^\infty\right)}{L}x + c_{e,0}^\infty \quad (23)$$

and

$$\phi(x,t) \approx \frac{D_e}{u_V c_A}e^{-\alpha^2\gamma^2 t}\left[\frac{\left(c_e^0 - c_{e,L}^\infty\right) - \left(c_e^0 - c_{e,0}^\infty\right)\cos\gamma L}{\sin\gamma L}\sin\gamma x + \left(c_e^0 - c_{e,0}^\infty\right)\cos\gamma x\right] + \frac{\left(\phi_L^\infty - \phi_0^\infty\right)}{L}x + \phi_0^\infty \quad (24)$$

Case (2). Second, consider the response of the SOFC when a load is introduced after it was initially in *open-circuit* conditions (no load). In such conditions $c_e(0, 0) = c_{e,0}^0$, $c_e(L, 0) = c_{e,L}^0$. Hence

$$c_e(x,t) = e^{-\alpha^2\gamma^2 t}\left[\frac{\left(c_{e,L}^0 - c_{e,L}^\infty\right) - \left(c_{e,0}^0 - c_{e,0}^\infty\right)\cos\gamma L}{\sin\gamma L}\sin\gamma x + \left(c_{e,0}^0 - c_{e,0}^\infty\right)\cos\gamma x\right] + \frac{\left(c_{e,L}^\infty - c_{e,0}^\infty\right)}{L}x + c_{e,0}^\infty \quad (25)$$

and

$$\phi(x,t) \approx \frac{D_e e^{-\alpha^2\gamma^2 t}}{u_V c_A}\left[\frac{\left(c_{e,L}^0 - c_{e,L}^\infty\right) - \left(c_{e,0}^0 - c_{e,0}^\infty\right)\cos\gamma L}{\sin\gamma L}\sin\gamma x + \left(c_{e,0}^0 - c_{e,0}^\infty\right)\cos\gamma x\right] + \frac{\left(\phi_L^\infty - \phi_0^\infty\right)}{L}x + \phi_0^\infty \quad (26)$$

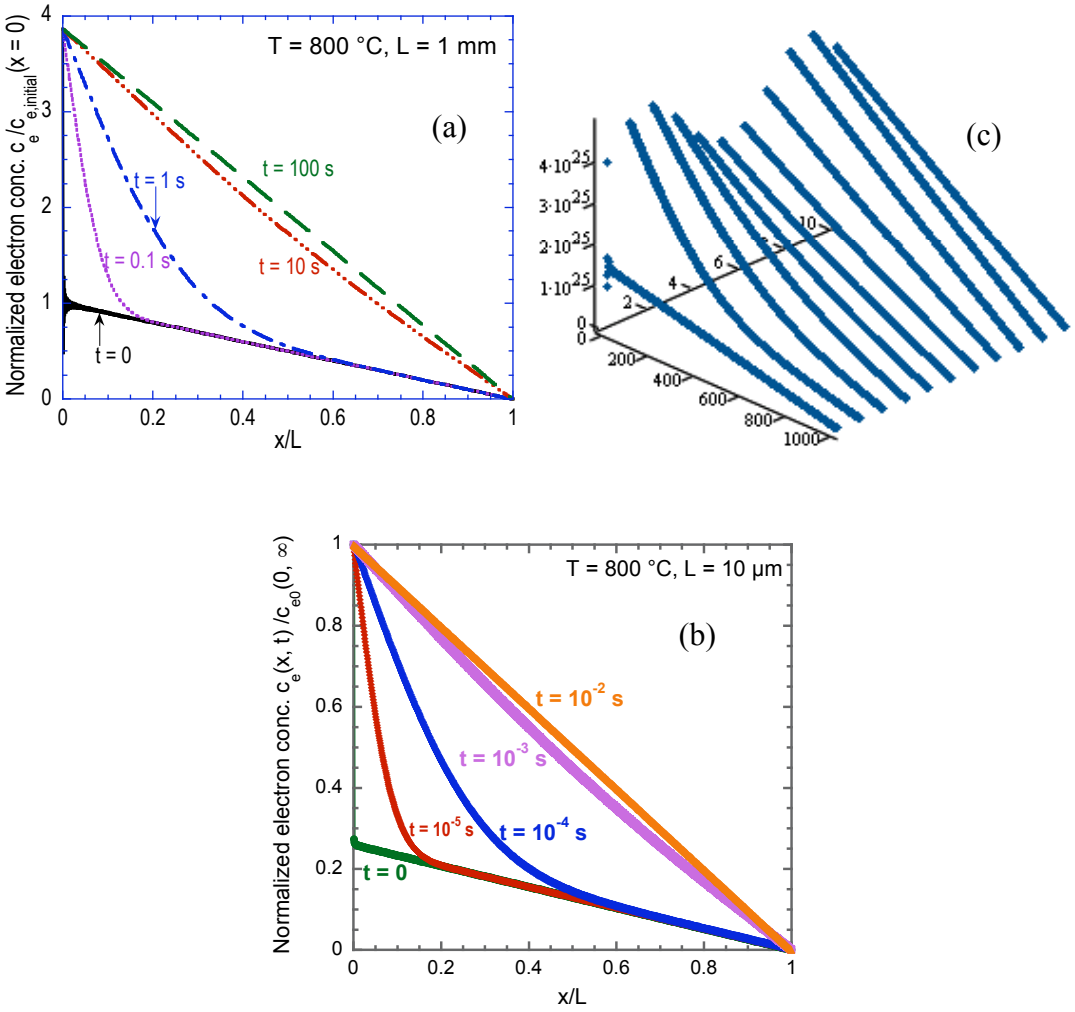

Figure 10. Time-dependent evolution at 800 °C of electron concentration profiles in a YSZ electrolyte (a) 1 mm thick, where the load voltage, Φ_{ext}, goes from *open-circuit* value to $\Phi_{th}/4$; (b) 10 μm thick, Φ_{ext} goes from *open-circuit* value to $\Phi_{th}/4$; and (c) 1 mm thick, Φ_{ext} has a 60 Hz sinusoidal *ripple*. Anode is at $x = 0$ ($P_{O_2} = 10^{-22}$ atm), cathode at $x = L$ ($P_{O_2} = 0.21$ atm).

Figure 10 shows the evolution of the electron concentration profiles in a YSZ electrolyte. In Fig. 10(a) a load (of voltage $\Phi_{th}/4$) is introduced to the SOFC, which was initially (at time, $t = 0$) in *open-circuit* conditions. The results show that while the boundary concentrations are established *instantly*, the concentration in the bulk lag behind, ostensibly limited by electron diffusivity and electrolyte thickness. In Fig. 10(b) the same conditions apply, except instead of a 1 mm thick electrolyte as in 10(a), we now have a 10 μm thick electrolyte. As one might intuit, the model shows that the response is much faster with the thinner electrolyte since the defects

have a much smaller distance to diffuse. In other words, the lag in the bulk observed in Fig. 10(a) is reduced. Finally, we note that the response time is proportional to the square of the thickness in accordance with classic diffusion models (thickness decreased by factor of 10^2, response time increased by factor of 10^4).

Figure 10(c) is a surface plot showing the spatial and temporal distribution of electron concentration, $c_e(x, t)$. In Fig. 10(c) a load is again introduced to the SOFC, but this time it carries a 60 Hz sinusoidal *ripple* with it. The effect and presence of the *ripple* is evident in the plot, which shows an initial response similar to Fig. 10a. However, after about 6 s, the lag is no longer evident even though the *ripple* persists. This is a result of the amplitude and frequency of the *ripple*. The amplitude is small enough not to cause great changes in the concentration gradient. While the time constant of the electrolyte (~4.5 s) is ~ 270 times the period of the *ripple*. Hence, the electrolyte does not have enough time to respond to the *ripple* in the bulk and the *ripple's* effect is seen only at the boundaries.

For transient defect transport, the total thickness of the MIEC, L, is a component of the time constant for the process such that the transient response of the MIEC depends exponentially on the electrolyte thickness. As the thickness of the electrolyte is reduced to 10 μm, the time scale reduces to ~0.05 s (approaching 60 Hz). Therefore, this provides important criteria (impact of improved performance with thinner electrolytes versus susceptibility to higher transient voltages or fuel composition variations) for SOFCs employed in transient conditions.

Extension of Continuum-Level Electrochemical Model to Chemical-Stability.

The continuum-level electrochemical model has also been applied to the chemical stability of YSZ/LSM and YSZ/LSCF interfaces. Figure 11 shows voltage across the LSM layer for various thickness ratios (L_B/L_A; L_A is the thickness of the YSZ layer, L_B is the thickness of the LSM layer) and operating conditions (V_{load}). Reasonably, as the thickness ratio increases so does the voltage across the LSM layer. Also, as the thickness ratio decreases (thinner LSM) the model predicts that the likelihood of lanthanum zirconate (LZ) formation (a resistive phase) at the LSM-YSZ interface increases.

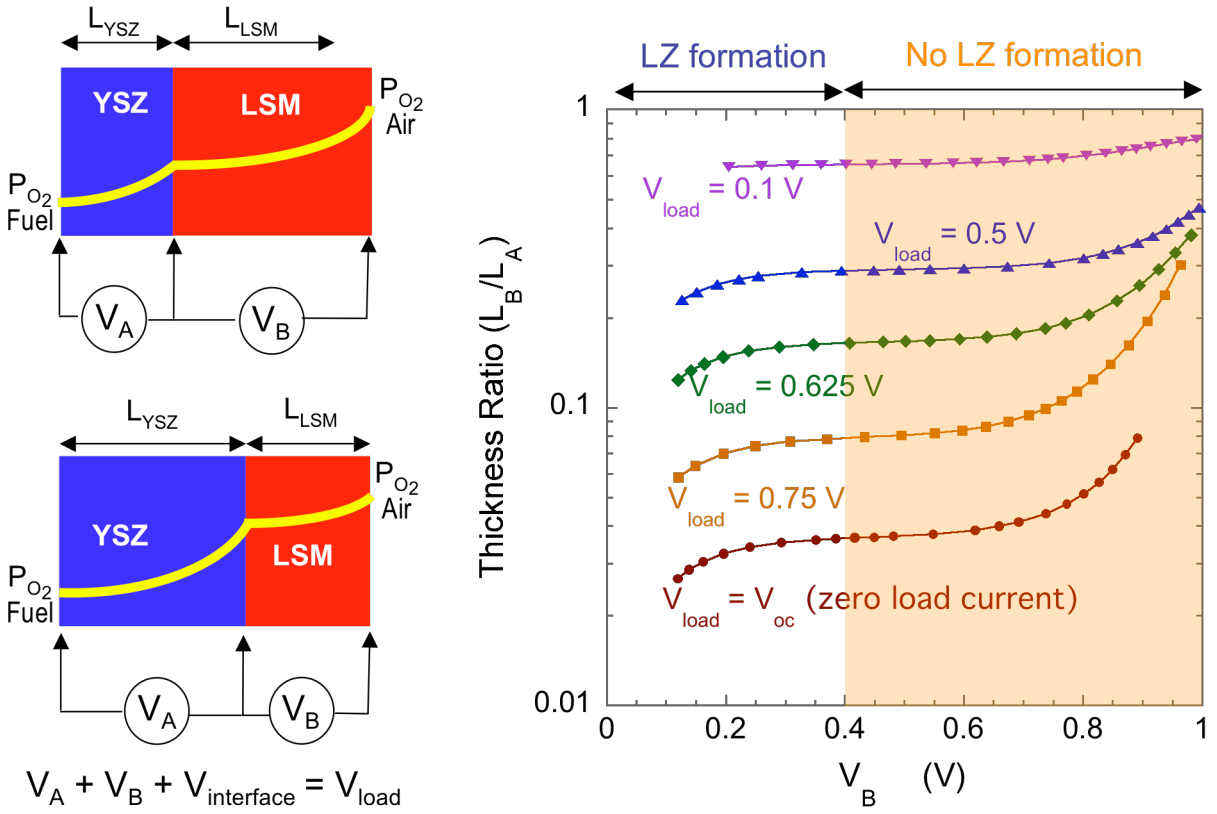

Figure 11. Voltage across the LSM layer for various thickness ratios (L_B/L_A; $L_A \equiv$ thickness of the YSZ layer, $L_B \equiv$ thickness of the LSM layer) and operating conditions (V_{load}); LZ ≡ lanthanum zirconate

By considering the reaction of LSM and YSZ to be described as follows

$$\underset{\text{cathode}}{La_{1-y}Sr_yMnO_3} + \underset{\text{zirconia electrolyte}}{\delta ZrO_2} + \underset{\text{gas phase}}{\tfrac{3}{4}\delta O_2} \rightarrow \underset{\text{weakened cathode}}{La_{1-y-\delta}Sr_yMnO_3} + \underset{\text{secondary phase}}{\tfrac{\delta}{2}La_2Zr_2O_7} + \tfrac{3}{2}\delta V_O^{\bullet\bullet} + 3\delta e' \qquad (27)$$

then one may write for the mass action constant K

$$K \approx \left[La_2Zr_2O_7\right]^{\frac{\delta}{2}} P_{O_2,\text{interface}}^{-\frac{3\delta}{4}} \qquad \text{or} \qquad \left[La_2Zr_2O_7\right]^{\frac{\delta}{2}} \approx K P_{O_2,\text{interface}}^{\frac{3\delta}{4}} \qquad (28)$$

and for the voltage drop across the LSM layer, V_B, we have

$$V_B \approx \frac{kT}{4q} \ln \frac{P_{O_2,x=L}}{P_{O_2,\text{interface}}} \qquad (29)$$

Hence one deduces that whenever the interfacial P_{O_2} is high (low V_B) there will be more LZ formation and for low interfacial P_{O_2} (high V_B) there will be less LZ formation. Moreover, if V_B is above the formation energy for LZ then no LZ will be produced at the interface.

The results further suggest a more pronounced dependence of V_B (and therefore the decomposition) on the thickness ratio for YSZ/LSCF due to ionic conduction in LSCF. Likewise, a more pronounced dependence is likely for GDC/LSM and GDC/LSCF because of electronic conduction in GDC. However, this is offset by the greater chemical stability of GDC relative to YSZ.

Extension of Continuum-Level Electrochemical Model to Thermo-Chemical Expansion

The introduction of point defects into a crystal lattice results in its expansion or contraction[12,18]. This phenomenon is the so called chemical expansion, α_{chem}. Measurement of the lattice constant, a, reveals that fluorite-structured oxides obey Vegard's law, i.e., a, is linearly dependent on c_a and c_v [12,18], therefore the thermo-chemical expansion may be written as follows

$$\frac{a-a_0}{a_0} = \underbrace{\theta \Delta T}_{\text{thermal expansion}} + \underbrace{a_0^{-1}\beta' c_a + \beta a_0^{-1} c_v}_{\text{chemical expansion}}$$

and, for isothermal conditions (i.e., $\Delta T = 0$), we have

$$\alpha_{chem} = \frac{a-a_0-\beta' c_a}{a_0} = \frac{\beta}{a_0} c_v \tag{30}$$

where a_0 is the lattice constant in the absence of defects; and the constant β and β' are the increase in lattice parameter due to defect formation from external equilibria (Eq. (10)) and doping, respectively. So, combining Eqs. (18) and (30) gives the *chemical expansion* as follows

$$\alpha_{chem} = \frac{\beta}{a_0}\left[\tfrac{3}{4} K_r^{\frac{1}{2}} P_{O_2}^{-\frac{1}{4}} + \left(\tfrac{1}{2} c_a\right)^{\frac{3}{2}}\right]^{\frac{2}{3}} \tag{31}$$

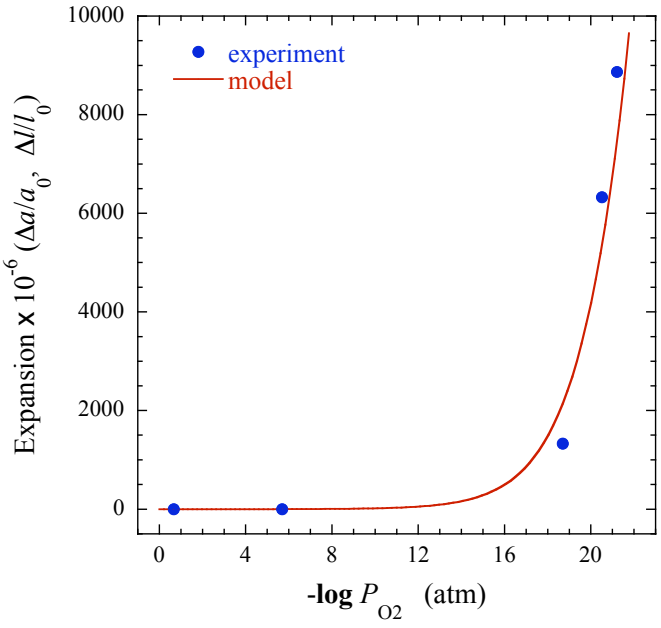

Figure 12. Chemical expansion of GDC; (●) expansion data from Bishop *et al.* [28], (−) model.

Chemical expansion (at equilibrium) does not involve defect transport. Hence, unlike electrical conductivity, the equilibrium constants (which control defect formation) for GDC are decoupled from the transport coefficients (defect diffusivities). The resultant expressions for the chemical expansion of GDC and YSZ are found in Table 1. We also modeled the chemical expansion of ceria, but, because defect association was included, a closed-form expression was not possible and the results were obtained numerically. The models were then experimentally validated by dilatometry as a function of P_{O_2}. Comparison of the model predictions to experimental results are given in Figs. 12-14.

Table 1. Expressions for thermo-chemical expansion of GDC and YSZ (P_{O_2} in atm, other quantities in SI units).

Material	Expression for Thermo-Chemical Expansion[a]
GDC	$\frac{\Delta l}{l} = 12.7\times10^{-6}\Delta T + \left(5.58\times10^{-9}P_{O_2}^{-\frac{1}{4}} + 8.94\times10^{-5}\right)^{\frac{2}{3}}$
YSZ	$\frac{\Delta l}{l} = 10.2\times10^{-6}\Delta T + \left(4.29\times10^{-15}P_{O_2}^{-\frac{1}{4}} + 1.87\times10^{-5}\right)^{\frac{2}{3}}$

[a] Values of the constants in the equations are applicable near 800 °C.

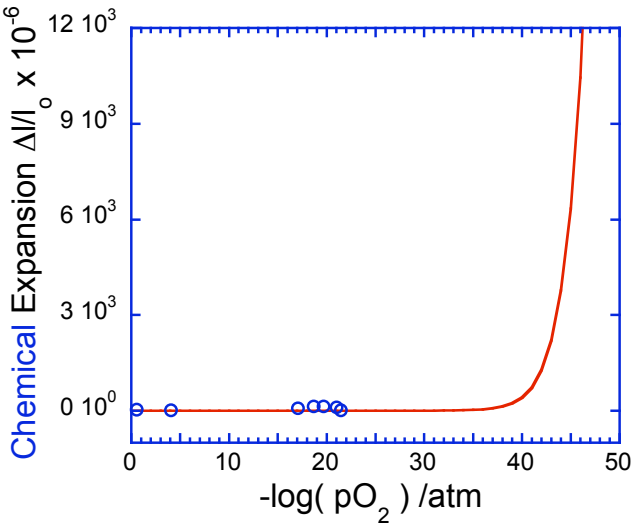

Figure 13. Chemical expansion of YSZ; (○) expansion data, (−) model.

Figure 12 shows Eq. (31) fitted to chemical expansion data[28] at 800 °C for GDC, $\beta \approx 1.73 \times 10^{-3}$ nm^4 [18]. A constant correction term, $\alpha_{chem,\ air} \approx \beta c_a/2a_0$, was subtracted from Eq. (31) to account for isobaric chemical expansion in air due to the temperature increase from room temperature to 800 °C. A good fit was obtained using $K_r = 1.3 \times 10^{-9}$ atm$^{1/2}$nm^{-9} which is the value obtained earlier, Fig. 4, from fitting Eq. (20) to thermogravimetric data from Wang *et al.*[11] for GDC.

Figure 13 shows that isothermal chemical expansion was not observed for YSZ, because the vacancy concentration remained constant in the P_{O_2} range of the experiment. Values of β, K_r and c_a appropriate for YSZ were substituted to obtain the fit. Nevertheless, the model predicts that chemical expansion of YSZ is a possibility in extremely reducing environments. Furthermore, this will shift towards higher P_{O_2} as the operating temperature increases.

We also modeled the chemical expansion of pure ceria as a function of P_{O_2}. However, it was necessary to include defect association of the species in the model[29]. Figure 14 shows a fit of our model to our chemical expansion data and that of Chiang *et al.*[30] for ceria at 800 °C. The same value for β was used as in the case of GDC with suitable values for the equilibrium constants. Again, a good fit was obtained, demonstrating the validity of our approach.

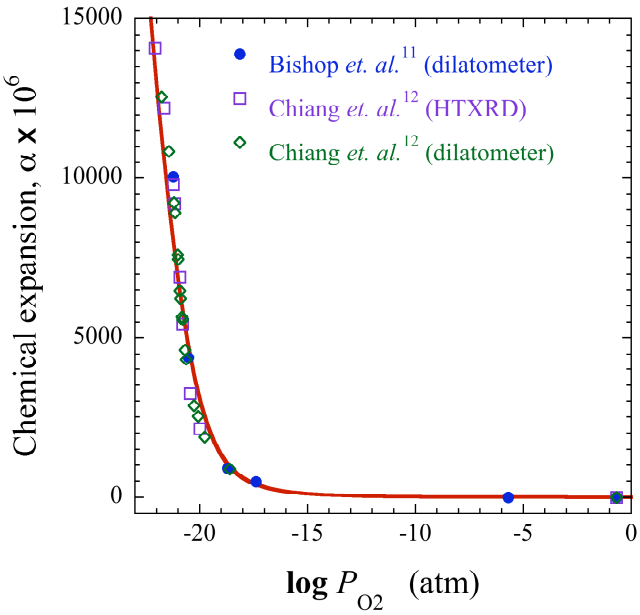

Figure 14. Chemical expansion of ceria; (●) dilatometer data from Bishop *et al.*[28], (□) high temperature XRD data from Chiang *et al.*[12], (◊) dilatometer data from Chiang *et al.*[30], (—) model

Extension of Continuum-Level Electrochemical Model to Elastic Modulus

We will now turn our attention to the mechanical properties: elastic modulus and fracture toughness. The bond energy, U, between atoms in a crystal, may be approximated by

$$U = \frac{b_r}{r^n} - \frac{b_a}{r^m} \tag{32}$$

where r is the interatomic distance (between nearest neighbor cation and anion), b_r and b_a are empirically determined constants for the repulsive and attractive components of the ionic bond energy in a perfect (defect free) crystal, respectively, n is the Born exponent and m arises from the Coulombic (attractive) forces. Setting the first derivative of Eq. (32) to zero and evaluating it at $r = r_{eq}$, the equilibrium interatomic distance, yields

$$\left.\frac{\partial U}{\partial r}\right|_{r=r_{eq}} = -n\frac{b_r}{r_{eq}^{n+1}} + m\frac{b_a}{r_{eq}^{m+1}} = 0 \qquad \text{or} \qquad \frac{b_r}{b_a} = \frac{m}{n} r_{eq}^{n-m} \tag{33}$$

The elastic modulus, E, may then be estimated from the second derivative of U, and substituting Eq. (33), as follows

$$E = \frac{1}{r_{eq}} \cdot \left.\frac{\partial^2 U}{\partial r^2}\right|_{r=r_{eq}} = b_r n(n-m)\frac{1}{r_{eq}^{n+3}} = b_a m(n-m)\frac{1}{r_{eq}^{m+3}} \tag{34}$$

Furthermore, since for the fluorite structure, $r_{eq} = \sqrt{3}\,a/4$, combining Eqs. (30) and (34) yields

$$E = E^*\left(\frac{\beta}{a_0}c_v + 1\right)^{-(n+3)} \qquad \text{where} \qquad E^* = b_r n(n-m)\left(\tfrac{\sqrt{3}}{4}a_0\right)^{-(n+3)} \tag{35a}$$

$$E = E^*\left(\frac{\beta}{a_0}c_v + 1\right)^{-(m+3)} \qquad \text{where} \qquad E^* = b_a m(n-m)\left(\tfrac{\sqrt{3}}{4}a_0\right)^{-(m+3)} \tag{35b}$$

and

$$\frac{b_r}{b_a} = \frac{m}{n}\left(\tfrac{\sqrt{3}}{4}a_0\right)^{n-m}\left(\frac{\beta}{a_0}c_v + 1\right)^{n-m} \tag{36}$$

Equation (35) provides us with the functional dependence of the elastic modulus on point defect concentration and P_{O_2}—through Eq. (18). Specifically, Eq. (35) predicts that the elastic modulus decreases as the oxygen lattice vacancy concentration increases. The isothermal elastic modulus of a perfect ($c_v = 0$) crystal, E^*, is constant, and n and m are not expected to change significantly when oxygen vacancies are introduced into the ceramic. Thus, from Eq. (36), it is clear that Eq. (35a) presumes that b_a changes with the introduction of point defects, while b_r remains relatively invariable. In other words, for any value of r, the introduction of oxygen vacancies in the lattice causes a reduction in the attractive energy (b_a/r^m), but has a relatively insignificant effect on the repulsive energy contribution (b_r/r^n) in the lattice.

Conversely, Eq. (35b) presumes that introducing point defects causes a much more significant change in b_r than b_a. That is to say, for any value of r, the introduction of oxygen

vacancies in the lattice causes an increase in the repulsive energy (b_r/r^n), but has a comparatively negligible effect on the attractive energy contribution (b_a/r^m) in the lattice.

It is important to emphasize that this is a simplification, clearly both b_r and b_a should vary with the defect population in the ceramic. However, the degree of change in each and, especially, their impact on the bond energy may differ significantly, thereby allowing one of the two constants to be treated as independent of the defect population. Moreover, the results are from a mathematical standpoint effectively the same, i.e., introduction of vacancies leads to a reduction of the overall energy; either by reducing the attractive component (b_r constant and b_a a function of c_v) or increasing the repulsive component (b_a constant and b_r a function of c_v). Thus, one only needs to fit Eqs. (35a) and (35b) to experimental data to determine which approximation is more suitable. Finally, since E^*, β and a_0 are all experimentally quantifiable constants, then for $n \neq m$ only one of Eq. (35a) or (35b) will produce accurate results for the given set of constants: n, m, E^*, β and a_0.

The resultant expressions for the elastic modulus of GDC and YSZ are found in Table 2. We also modeled the elastic modulus of ceria, but, because defect association was included, a closed-form expression was not possible and the results were obtained numerically. Experimental details are given in subsequent section on mechanical properties. Comparison of the model predictions to experimental results are given in Figs. 15-17.

Figure 15 shows Eq. (35a) fitted to elastic modulus data[14] at 800 °C for GDC, again $\alpha_{chem,air} \approx \beta c_a/2a_0$ was subtracted from α_{chem} to account for isobaric chemical expansion in air due to the temperature increase from room temperature to 800 °C. Since elastic modulus, like

Table 2. Expressions for the elastic modulus dependence on P_{O_2} for GDC and YSZ at 800 °C (P_{O_2} in atm, all other quantities in SI units).

Material	Expression for Elastic Modulus
GDC	$E = \left[\left(2.09\times10^{-10}P_{O_2}^{-\frac{1}{4}} + 3.36\times10^{-6}\right)^{\frac{2}{3}} + 0.112\right]^{-12}$ (Pa)
YSZ	$E = \left[\left(1.62\times10^{-16}P_{O_2}^{-\frac{1}{4}} + 7.05\times10^{-6}\right)^{\frac{2}{3}} + 0.113\right]^{-12}$ (Pa)

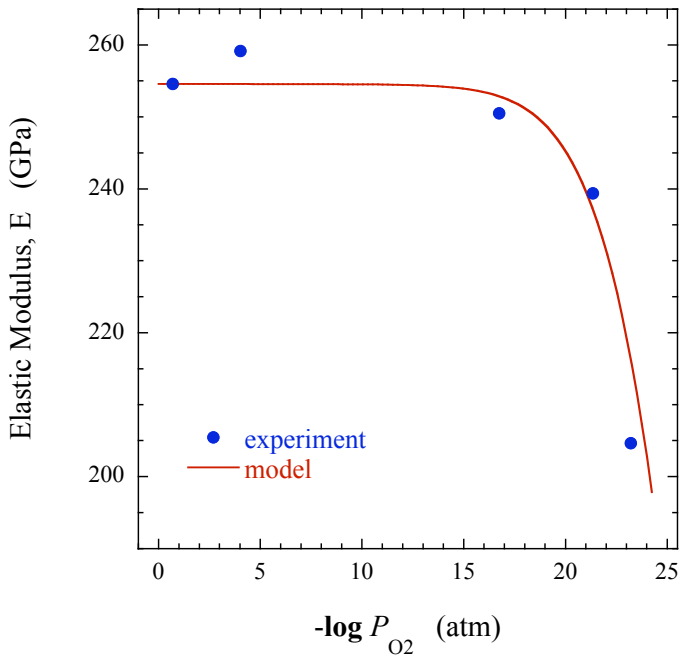

Figure 15. Variation of the elastic modulus with P_{O_2} for GDC; (●) nano-indentation data from Wang *et al.*[31] [13], (–) model.

chemical expansion, is dependent on the lattice constant, a, the same parameters ($c_a \approx 1.25$ nm^{-3}, $\beta \approx 1.73 \times 10^{-3}$ nm^4 and $K_r = 1.3 \times 10^{-9}$ atm$^{1/2}$nm^{-9}) used earlier for the chemical expansion data are applied here. The ability to use unchanged parameters to fit both independent experiments demonstrates the validity of the approach developed herein and the important role played by defects in the thermo-mechanical properties of ceramics.

As Fig. 15 shows, an excellent fit of the model, Eq. (35a), was obtained for the dependence of elastic modulus on P_{O_2} for GDC using $n = 9$, which is typical for ceramics. Fitting the elastic modulus data with Eq. (35b) using $m = 1$, which is typical for ceramics, resulted in an overestimation (not shown) of the elastic modulus of GDC. We, therefore, conclude that changes in b_r arising from increasing the point defect concentration have a greater influence on the bond energy than corresponding changes in b_a. Hence Eq. (35a) is the appropriate model for the dependence of elastic modulus on point defect concentration.

Again, we were also able to model the elastic modulus of pure ceria as a function of P_{O_2} by including defect association of the species in the model[29]. Figure 16 shows a fit of this model

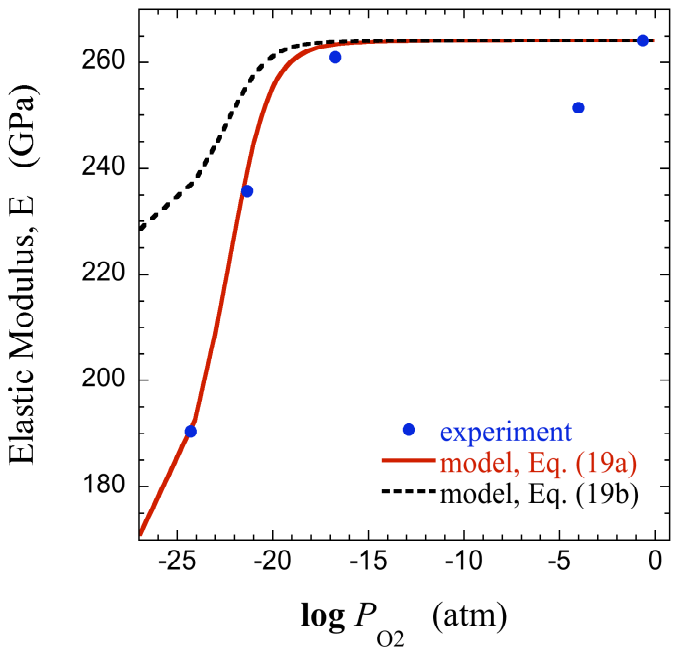

Figure 16. Variation of the elastic modulus with P_{O_2} for ceria; (●) nano-indentation data from Wang *et al*. [ ]; (—) model, Eq. (19a); (---) model, Eq. (19b).

to elastic modulus data for ceria at 800 °C[31]. Since elastic modulus, like chemical expansion, is dependent on the lattice constant, a, the same parameters used earlier for the chemical expansion data are applied here. As before, a good fit was obtained, demonstrating the validity of our approach.

Figure 16 also shows that fitting the elastic modulus data with Eq. (35b) using $m = 1$ (typical for ceramics) resulted in an overestimation of the elastic modulus of ceria. We, therefore, conclude that changes in the repulsive component, b_r, arising from increasing the point defect concentration have a greater influence on the bond energy than corresponding changes in the attractive component, b_a. Hence Eq. (35a) is the appropriate model for the dependence of elastic modulus on point defect concentration.

Figure 17 shows, an excellent fit of the model, Eq. (35a), was also obtained for the dependence of elastic modulus on P_{O_2} for YSZ. Values of E^* β, K_r and c_a appropriate for YSZ were substituted to obtain the fit. The model predicts that a reduction in the elastic modulus of YSZ is a possibility in extremely reducing environments. Furthermore, as discussed earlier for chemical expansion, this will shift towards higher P_{O_2} as the operating temperature increases.

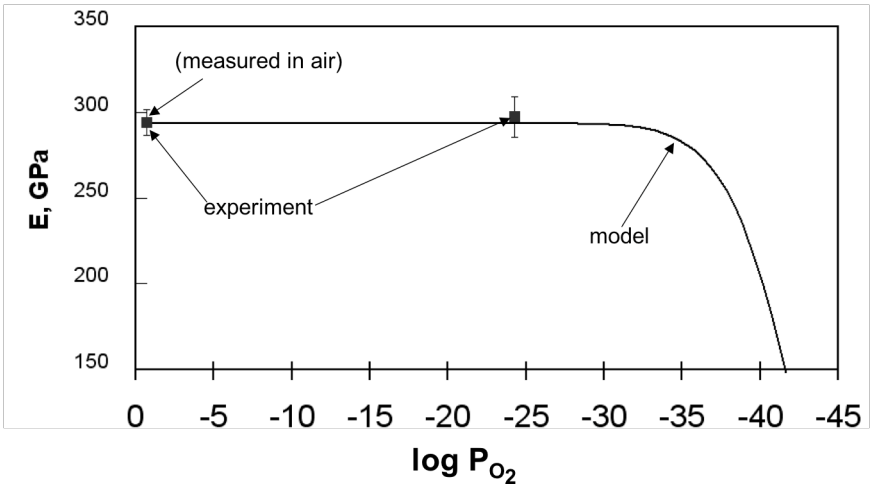

Figure 17. Variation of the elastic modulus with P_{O_2} for YSZ; (■) nano-indentation data from Wang *et al*. [ ]; (—) model.

Incorporation of Microstructural Effects into Continuum-Level Electrochemical Model

The effect of polycrystallinity on the modeled material properties is negligible as long as the porosity, ξ, is small. Nevertheless, the effect of polycrystallinity can be accounted for using the method of Wagh *et al*. [32], as follows

$$\Theta = \Theta_0 (1-\xi)^m \tag{37}$$

where Θ is the bulk property under consideration and m is an exponent related to the tortuosity of the connected pores of the material. For example combining Eq. (37) with Eq. (35a) would yield, for the elastic modulus

$$E = E^* \left(\frac{\beta}{a_0} c_v + 1 \right)^{-(n+3)} (1-\xi)^m \tag{38}$$

While beneficial for the mechanical properties themselves, unfortunately, the samples studied in this project, all had low porosity and so we were not able to validate this approach.

Software packaging of Continuum-Level Electrochemical Model

Software modules for the continuum-level electrochemical model were developed. They are available to the teams at ORNL, NETL and PNNL and to the SECA industrial teams for testing to determine their compatibility with existing failure analysis software. Two languages were used, C++, because it is the industry standard, and PHP, because of its web oriented features.

MECHANICAL PROPERTIES

Elastic Modulus: Bulk

Samples were carefully prepared to limit the variation of porosity and porosity distribution from one sample to the other. The relative densities and the average grain sizes of the as-sintered samples for all three materials are shown in Table 3. For the as-sintered ceria samples, they all had density higher than 94 % with an average grain size of 13 μm. GDC samples had slightly higher density up to 98 % with an average grain size of 5 μm. Finally, YSZ samples were more than 99 % dense with an average grain size of 4 μm.

After reduction under low P_{O_2}, micro-cracks appeared on the pure ceria sample surface prior to loading. When the P_{O_2} was less than 10^{-19} atm, some samples broke in the high temperature reduction process. The development of micro-cracks under severe reduction is caused by the internal stresses resulting from the lattice expansion difference between the reduced surface and the unreduced interior[33]. In order to understand the distribution of the micro-cracks, the cross section of one sample heat treated under $P_{O_2}=4.5\times10^{-22}$ atm was polished and imaged using SEM. Micro-cracks were observed throughout the entire thickness. There was no obvious difference in the size and distribution of the micro-cracks as a function of the distance from the exposed surface to the middle. Fig. 18 shows an SEM image of the micro-cracks in the middle of a sample. The arrows in the figure indicate the positions of the micro-cracks.

For intrinsic elastic modulus, a typical indent with the associated load-displacement curve are shown in Fig. 19. The high resolution nano-indent topography image (Fig. 19a) was recorded using scanning probe microscopy for an area of 5×5 μm. This indent is about 0.6 μm in

Table 3. Relative density and average grain size of the as-sintered samples

Composition	Relative density (%)	Average grain size (μm)
CeO_2	>94%	13
$Gd_{0.1}Ce_{0.9}O_{1.95}$	>98%	5
$(Y_2O_3)_{0.08}(ZrO_2)_{0.92}$	>99%	4

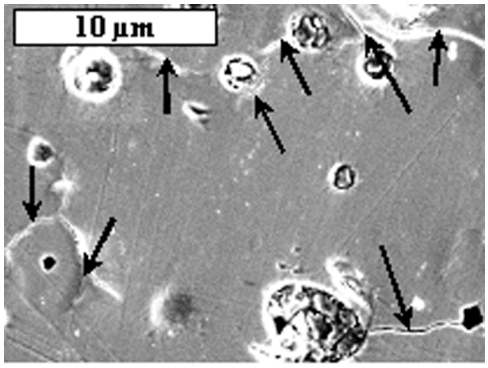

Figure 18. SEM image of the micro-cracks on a polished surface of the sample heat treated in P_{O_2} = 4.5×10^{-22} atm. The arrows in the image indicate the micro-cracks.

length with a contact depth of 120 nm. The nano-indents were distributed in a 7×7 or 10×10 grid with 5 µm separation from each other. A total area with more than 16 grains was covered for ceria and with 45 to 70 grains was covered for GDC and YSZ samples. The average elastic moduli for samples tested are given in Table 4. Since the indents were introduced in many grains, the small variation in the elastic modulus for each sample indicates that the tested oxides with the fluorite structure are elastically isotropic. Comparing the measured elastic modulus for the air treated samples obtained by nano-indentation, we find that the elastic modulus values for pure ceria and GDC are both approximately 33% higher than the bulk values reported by K. Sato *et al*.[34]. In the case of YSZ, our data are 18% lower than the nano-indentation results on single-crystal YSZ reported by B. Savoini[35] but 10% higher than the dynamic bulk elastic modulus of 222 GPa for porosity-corrected 6.5 mol% YSZ reported by J. W. Adams *et.al.*[36] and A. J. A.

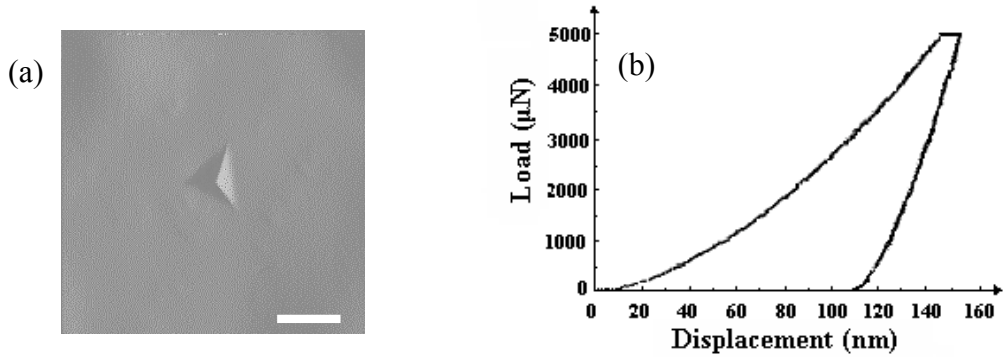

Figure 19. Nano-indent image on the as-sintered pure ceria sample (a) and the corresponding load-displacement curve (b).

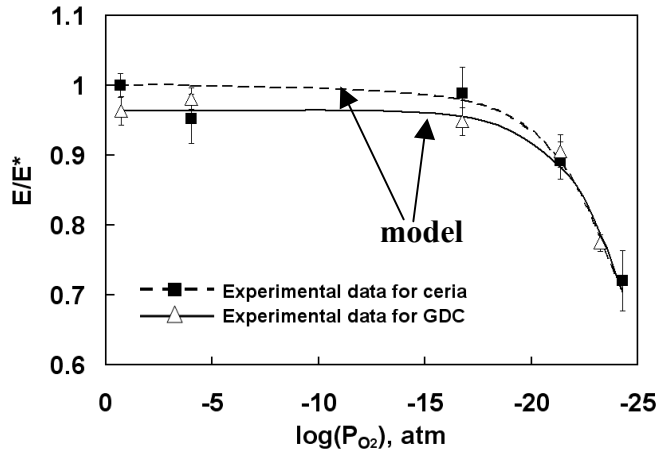

Figure 20. Experimental results compared predictions from the model (Eq. (35a)), showing the variation of normalized elastic modulus (*E/E**) of pure ceria and GDC equilibrated at different partial pressure of oxygen (P_{O_2}) at 800 °C and then fast cooled to room temperature.

Winnubst[37]. Besides the composition and microstructure differences, bulk elastic modulus measurements using conventional mechanical test methods have limitations of strain measurement and fixture/sample contact, which normally yield lower values.

The model, Eq. (35a), is fitted to elastic modulus data for GDC and ceria in Fig. 20. Since elastic modulus, like chemical expansion, is dependent on the lattice constant, a, the same parameters ($c_a \approx 1.25$ nm^{-3}, $\beta \approx 1.73 \times 10^{-3}$ nm^4 and $K_r = 1.3 \times 10^{-9}$ atm$^{1/2}$nm^{-9}) used earlier for the chemical expansion data are applied here. The ability to use unchanged parameters to fit both independent experiments demonstrates the validity of the approach developed herein and the important role played by defects in the thermo-mechanical properties of ceramics.

Figure 20 shows the elastic moduli for pure ceria and GDC remain almost constant when P_{O_2} is higher than 10^{-17} atm, but decrease drastically (approximately 28%) as the P_{O_2} is reduced

Table 4. Elastic modulus results for heat treatments under different P_{O_2} .

		CeO_2	$Gd_{0.1}Ce_{0.9}O_{1.95}$	$Zr_{0.92}Y_{0.08}O_{1.96}$
E (GPa)	@ 0.22 atm	264.1±5.5	254.6±6.4	243.3±7.5
	@ 9.50x10^{-05} atm	251.5±11.1	259.2±4.9	
	@ 1.80x10^{-17} atm	261.0±12.4	250.5±6.5	
	@ 4.50x10^{-22} atm	235.7±8.8	239.3±7.5	
	@ 6.0x10^{-24} atm		204.7±3.8	
	@ 5.10x10^{-25} atm	190.4±14.9		246.2±11.7

down to 5.1×10^{-25} atm. However, the change in the elastic modulus of YSZ within the studied P_{O_2} range and at temperature of 800 ^{o}C was insignificant. These observations are consistent with the change of color, which correlates with the concentration of defects.

When oxygen vacancies are introduced at low oxygen partial pressures in fluorite-structured MO_2 oxides, the charge neutrality is restored by the creation of M^{3+} defects. Likewise, substitution of M^{4+} with a lower valance cation through doping causes formation of oxygen vacancies in the lattice. In both cases, owing to the presence of the lower valance cations, the result is an increase in average bond length. This change in bond length is expected to result in a reduction in the intrinsic elastic modulus[38].

Consistent with the experimental observation, this relationship predicts that elastic modulus should decrease with increasing lattice parameter owing to the introduction of oxygen vacancies. Assuming that temperature has insignificant effect on elastic modulus and lattice parameter ratios, an evaluation of Eq. (35) would shed light on the nature of bond modification.

As Fig. 20 shows, an excellent fit of Eq. (35a) was obtained for the dependence of elastic modulus on P_{O_2} for GDC using $n = 9$, which is typical for ceramics. Fitting the elastic modulus data with Eq. (35b) using $m = 1$, which is typical for ceramics, resulted in an overestimation of the elastic modulus of GDC. We, therefore, conclude that changes in b_r arising from increasing the point defect concentration have a greater influence on the bond energy than corresponding changes in b_a. Hence Eq. (35a) is the appropriate model for the dependence of elastic modulus on point defect concentration.

Since YSZ samples were not affected by the heat treatment, we analyzed the data for pure ceria and GDC. In order to evaluate the exponent in Eq. (35) we used the lattice parameter values from studies by Chiang *et al*.[30] and Wang *et al*.[39], where powder materials were heat treated under conditions similar to our experiments. The values for E^* and a_0^* were taken as the elastic modulus and lattice parameter for air treated pure ceria, respectively. Since the lattice parameters in references 30 and 39 were measure at the 800 °C, we corrected the values to room temperature using the expansion coefficient parameter given in reference 18. However, this correction did not change the lattice parameter ratio noticeably. The variation of the normalized elastic modulus as a function of the lattice parameter ratio is shown in Fig. 21. The data fit very

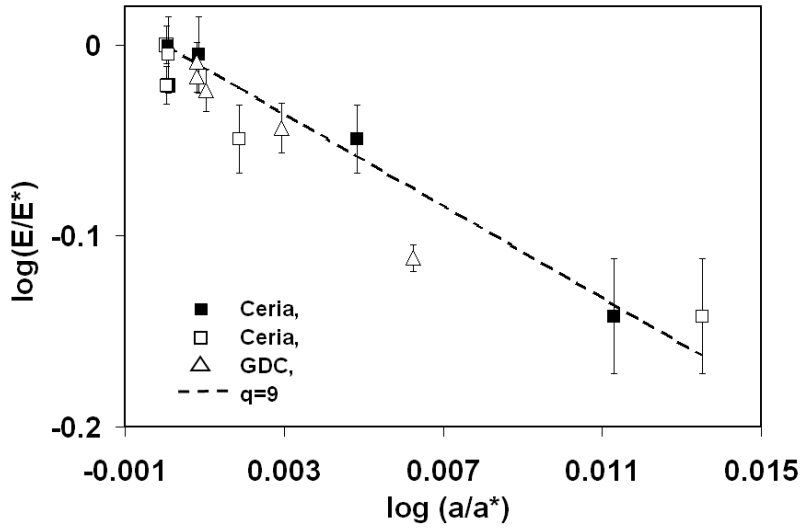

Figure 21. Normalized elastic modulus (*E/E**) as a function of the normalized lattice parameter (a/a*) for pure ceria and GDC. The symbols represent the experimental data with the elastic modulus measured in this work the and lattice parameter extrapolated from references 30 and 39. The dashed line has a slope of -12 and corresponds to n=9 in Eq. (35).

well with the line corresponding to n = 9, which suggests that the introduction of the defects modifies the attractive forces in the fluorite-structured oxides.

Elastic Modulus: Polycrystalline

For bulk elastic modulus test, it needs to be pointed out that in the absence of elastic anisotropy, the presence of grain boundary in polycrystalline samples is not expected to affect the elastic modulus as significant as pores and micro-cracks. All the tests were carried out within two days after the heat treatment process to minimize the re-oxidation effects. The results of bending tests for elastic modulus as well as the number of samples tested are shown in Table 5. The elastic modulus values were reproducible among several tests from sample to sample for each condition with the maximum variation of 7 % for the air treated ceria. Comparing the average elastic modulus measured by bending tests with those measured by nano-indentation for the air treated condition, the bending test results were 30 % lower for pure ceria, 26 % lower for GDC and 20 % lower for YSZ. This difference is related to be the effects of porosity and possibly experimental errors. However, the bulk elastic modulus results measured by bending

tests of this work are comparable to the literature reported bending modulus values for both ceria and GDC[34].

As shown in Table 5, bulk elastic modulus could not be evaluated in bending when the oxygen partial pressure was on the order of 10^{-19} atm due to severe micro-cracking. Most of the bending samples for ceria and GDC did not survive the reduction treatment for P_{O_2} of 10^{-22} atm and 10^{-24} atm. The survival rate became less as the oxygen partial pressure was decreased. Furthermore, the fracture loads for the ceria and GDC samples that survived the reduction treatment were too low (less than 2 lbs) for evaluating the elastic moduli. It should be mentioned that it is very difficult to control oxygen partial pressure continuously over several orders of magnitude. In other words, although 10^{-20} atm was not the lowest oxygen partial pressure we could achieve for bending samples, other heat treatments at specific P_{O_2}'s between 10^{-20} atm and 10^{-22} atm was not achievable.

Consistent with the intrinsic elastic modulus obtained by nano-indentation, the bulk bending modulus results reveal that the elastic modulus for GDC and ceria is significantly decreased after reduction treatment under 8.8×10^{-20} atm. While not as extreme, the reduction treatment reduced the elastic modulus of the YSZ samples by 7%.

Fig. 22 presents a detailed comparison of the oxygen partial pressure on the elastic modulus as evaluated by both techniques for all three materials. The moduli measured by these two methods were normalized by the respective elastic modulus for air treated samples for the purpose of comparison. The reduction treatment effect on the elastic modulus of bulk ceria was

Table 5. Bulk elastic modulus for heat treatments under different P_{O_2} evaluated by four-point-bend tests.

Materials	Various oxygen partial pressure P_{O_2}, atm		
	0.22	3.4×10^{-04}	8.8×10^{-20}
CeO_2	183.8±12.6 (6 samples)	196.3 (2 samples)	151.4 (2 samples)
$Gd_{0.1}Ce_{0.9}O_{1.95}$	188.8 (2 samples)	180.3 (2 samples)	----
$(Y_2O_3)_{0.08}(ZrO_2)_{0.92}$	192.3 (2 samples)	189.0 (1 sample)	177.9±2.3 (3 samples)

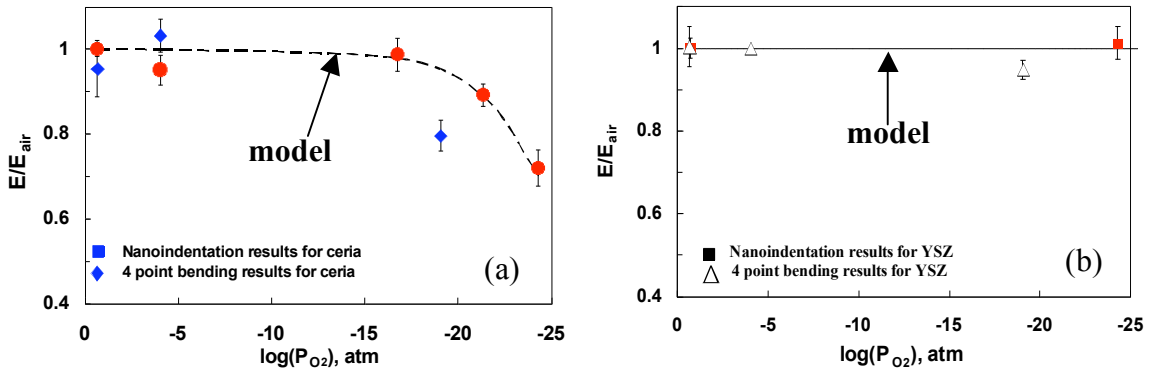

Figure 22. Relative elastic modulus (E/E_{air}) as a function of P_{O_2} compared with model, (Eq. (35a)) predictions for ceria (a) and YSZ (b).

more pronounced (Fig. 22) than the effect on elastic modulus by nano-indentation. This difference can be attributed to the micro-crack formation during the low P_{O_2} reduction process. One could consider this in terms of the effect of porosity, Eq. (38). However, since the number of micro-cracks is also a function of P_{O_2} it is difficult analytically to separate the effect of either factor on the modulus.

Since the decrease of the elastic modulus values by nano-indentation tests was not significantly affected by micro-cracking, it can be concluded that the variation of the intrinsic elastic modulus with oxygen partial pressure is mainly due to point defect formation. However, the decrease of the bulk elastic modulus after reduction treatment measured by bending includes the effect of both point defect formation and the micro-cracks and hence a more pronounced decrease in elastic modulus was observed.

Fracture Properties

Flexural Strength. The flexural strength test results, as a function of the oxygen partial pressure, are given in Table 6. The variation in the flexural strength test results was small (less than 10%) for samples heat treated at low P_{O_2} as well as those heat treated in Ar. However, the strength of the air treated samples varied noticeably from sample to sample (> 20%). Comparing the mean values, the flexural strength decreased significantly as a result of the reduction process.

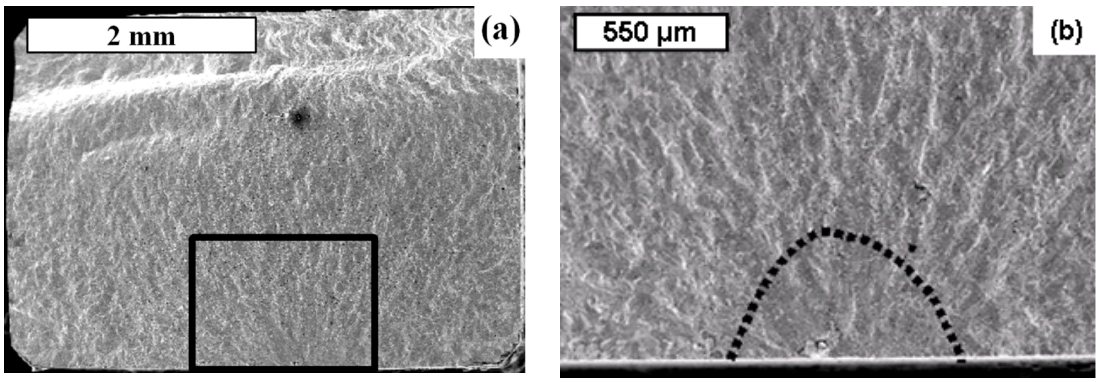

Figure 23. SEM image of the fracture surface (a) for a bending sample with σ_f = 96 MPa after heat treatment in air (P_{O_2} = 0.21 atm). (b) is the higher magnification image of the box area in (a). The dotted line in (b) shows the typical mirror zone for brittle fracture surface.

The room temperature mean flexural strength dropped from 127 MPa for air treated samples to almost no strength (< 4 MPa) for dry hydrogen ($P_{O_2} = 4.8\times10^{-24}$ atm) reduced samples.

The fracture surfaces of the flexural test samples showed distinct differences between air treated and low P_{O_2} treated samples. The samples heat treated in air exhibited classic brittle fracture patterns (see Fig. 23a) with one crack initiation site originating from surface imperfections, followed by a mirror zone (dotted region in Fig. 23b) and a hackle zone spreading outward from the crack origin.

However, no single distinct crack initiation origin was found on the fracture surface of the samples heat treated in low P_{O_2} atmospheres ($P_{O_2} < 10^{-19}$ atm). As shown in Fig. 24a, for a sample heat treated under 8.8×10^{-20} atm, although crack propagation direction can be identified through the river marks to be from the bottom of the image to the top, there is no distinct crack

Table 6. Room Temperature Flexural Strength Test Results.

Heat Treatment Condition	P_{O_2}, atm.	Number of Samples Tested	Approximate Composition	σ_f, MPa
H_2	4.8×10^{-24}	1[a)]	$CeO_{1.825}$ [c)]	<4
H_2 /H_2O	2.3×10^{-22}	2[b)]	$CeO_{1.877}$ [c)]	8
H_2 /H_2O/Argon	8.8×10^{-20}	4	$CeO_{1.991}$ [c)]	41±4
Argon	3.4×10^{-4}	3	CeO_2 [c)]	137±8
Air	0.21	4	CeO_2	127±30

a) 5 samples were heat treated, 4 samples broke during high temperature reduction and only one sample could be tested.
b) 3 samples were heat treated, however one sample broke during the high temperature reduction.
c) The composition is extrapolated from Bevan and Kordis[40]. The heat treatment under argon does not create significant amount of oxygen vacancies[38].

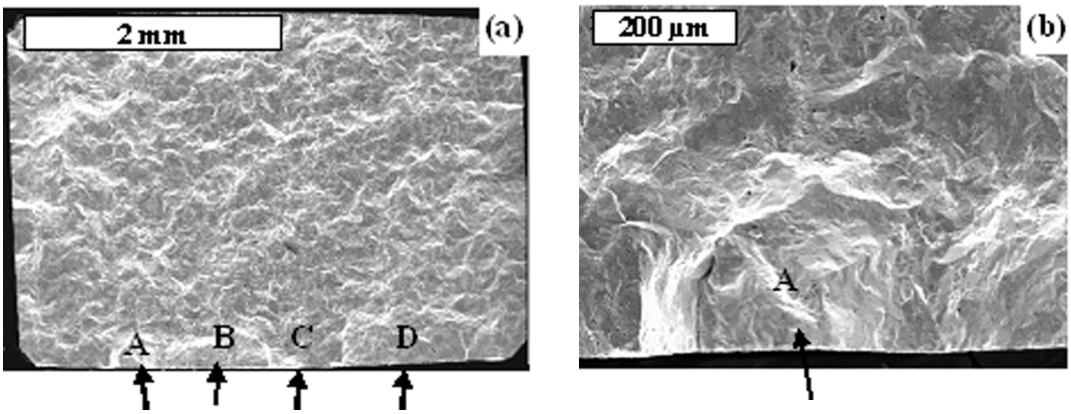

Figure 24. SEM image of the fracture surface (a) for a bending sample with σ_f = 44 MPa after heat treatment in H_2/H_2O/Argon ($P_{O_2} = 8.8\times10^{-20}$ atm). (b) is a higher magnification image of zone A.

origin as shown in Fig. 23. On the other hand, near the edge, where crack was initiated, several fracture zones that had developed on different levels can be identified. These zones are marked as A, B, C and D in Fig. 24a and a higher magnification of zone A is given in Fig. 24b. The size of these zones is approximately 200 to 800 μm, which is much larger than the grain size or the microcracks formed upon heat treatment (see Fig. 18). However, the microcracks are anticipated to act as crack initiation sites for these fracture zones. During loading, the pre-existing microcracks with favorable size (largest) and orientation (perpendicular to the loading direction) will initiate fracture. Since fracture zones developed by the propagation from different microcracks may lie on different planes, eventually, they will join each other by fracturing the ligament left between them. This process causes the formation of ridges that identifies each zone. It also shows in Fig. 24b that one large microcrack assisted the joins of initiated cracks and became the left margin of zone A.

The basic equation for fracture strength of ceramics, σ_f, based on the Griffith's theory, can be expressed as Eq. (39)[41].

$$\sigma_f = \left(\frac{2E'\gamma_i}{\pi C_0}\right)^{\frac{1}{2}} \tag{39}$$

where *E'* identifies with elastic modulus (E) in plane stress and ($E/(1-\nu^2)$) in plane strain with ν Poisson's ratio. The strength is therefore controlled by three basic parameters, which are the elastic modulus, E, the fracture surface energy for crack initiation, γ_i, and the initial flaw size, C_0.

From the previous section the elastic modulus of pure ceria decreased about 30% after reduction under $P_{O_2}= 4.5\times10^{-22}$ atm compared to the value after heat treatment in air[38,42]. This drop in elastic modulus alone obviously can not explain the 90% strength reduction given in Table 6. On the other hand, the presence of defects particularly on the surface is crucial to the results of flexural tests. The flexural strength is controlled by crack initiation process through, γ_i, and defect size, C_0. The toughness results suggest that γ_i may indeed increase after reduction treatment. Therefore, the change in fracture strength must be associated with the initial defect size. For the air treated samples, the processing defects (such as pores) on or near the surface control the measured strength. Heat treatment in low P_{O_2}conditions causes the formation of many microcracks, much larger and sharper than the processing defects. Therefore, the decreased flexural strength of ceria after heat treatment in a reduced atmosphere can be explained by the increase in the C_0 value. Furthermore, σ_f varies inversely with the square root of C_0, and therefore the variation in σ_f with defect size decreases as C_0 increases. In air treated samples, the defect size is relatively small and consequently the strength may vary significantly from one sample to another (see Table 6). In contrast, the multiple crack initiation behavior (see Fig. 24) and the consistency of the flexural strength values (see Table 6) for samples heat treated in low P_{O_2} are associated with the presence of relatively large micro-cracks in these samples.

Fracture Toughness. The crack length used for calculating the fracture toughness was determined by studying the fracture surfaces of Chevron-notched samples. The fracture surfaces showing the extent of stable pre-cracks for the sample heat treated in air (P_{O_2}=0.21atm) and H_2/H_2O ($P_{O_2}=1.5\times10^{-20}$ atm) are presented in Fig. 25. The transition of stable pre-crack to unstable fracture for the sample heat treated in air is not as distinct as the sample heat treated in hydrogen. The transition front (dashed line in Fig. 25a) of the air treated sample was distinguished from the low magnification SEM image based on the distinct contrast between the two regions when the area within the notch was in focus. The stable pre-crack front for the hydrogen treated sample was easily identified as shown in Fig. 25b. Within the stable crack

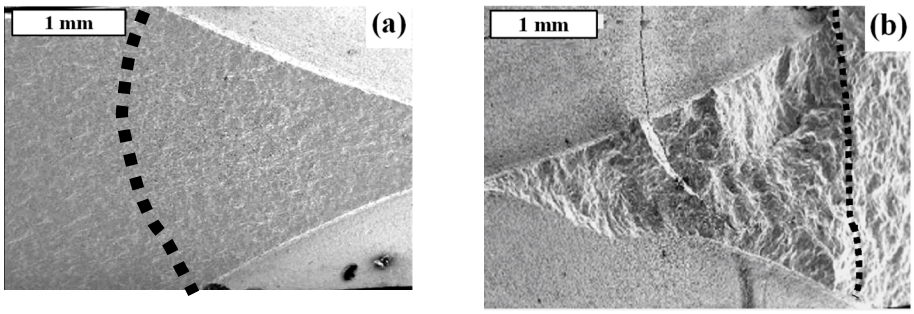

Figure 25. The stable pre-crack within the chevron-notched section for the sample heat treated (a) in air (P_{O_2}=0.21 atm) and (b) in H_2/H_2O (P_{O_2}=1.5×10^{-20} atm). The dashed lines show the stable to unstable crack transition fronts.

region, the sample heat treated in hydrogen showed significant roughness in comparison to the sample heat treated in air.

The fracture toughness test results as a function of oxygen partial pressure are shown in Table 7. The results were consistent for each heat treatment condition and K_{51C} values deviated within 6% with multiple tests. The fracture toughness data showed that the as-sintered, air treated and N_2 treated samples have similar room temperature K_{51C} values with variations within the test error. However, surprisingly, the K_{51C} increased as much as 30 to 40% for the samples heat treated in a reduced atmosphere (P_{O_2}=1.5×10^{-20} atm – 4.5×10^{-22} atm).

For the fracture toughness tests with Brazilian disc samples, crack initiation is not as crucial as in flexural tests and crack propagation controls the test results. The fracture toughness can be expressed in terms of the critical elastic energy release rate, G_C, and elastic modulus, E as

$$K_{IC} = \sqrt{E \cdot G_c} \tag{22}$$

Table 7. Room Temperature K_{51C} Test Results.

Heat Treatment Condition	P_{O_2}, atm.	Number of Samples Tested	Approximate Composition	K_{51C}, MPa•m$^{1/2}$
H_2/H_2O [a)]	4.5×10^{-22}	2[c)]	$CeO_{1.899}$ [d)]	1.32
H_2/H_2O [b)]	1.5×10^{-20}	2	$CeO_{1.981}$ [d)]	1.40
N_2	4.5×10^{-6}	1	CeO_2 [d)]	0.92
Air	0.21	3	CeO_2	0.96±0.05
As-sintered	-------	1	CeO_2	0.91

a) and b) used different H_2/H_2O ratio.
c) A total of 3 samples were heat treated, one sample broke during the high temperature reduction.
d) The composition is extrapolated from Bevan and Kordis[40], heat treatments in N_2 and air do not significantly increase the oxygen vacancy concentration[38].

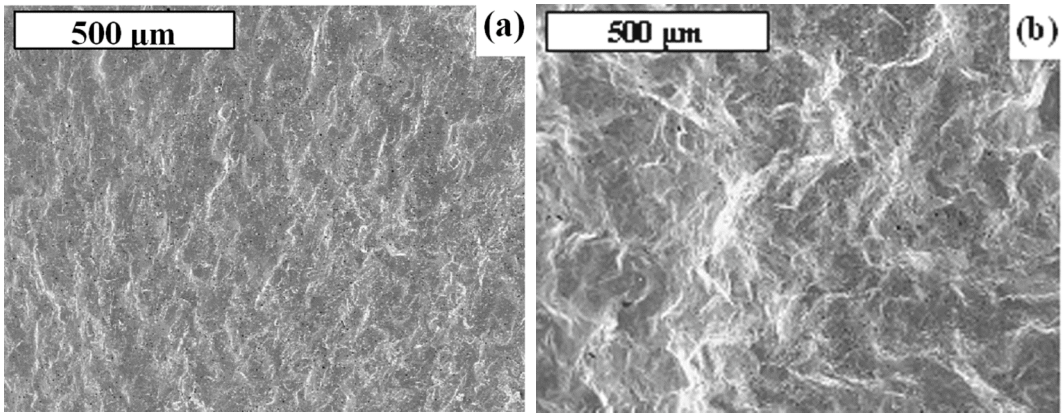

Figure 26. Comparison of the fracture surface roughness. (a) the higher mage of the hackle zone of a bending sample with heat treatment in air (P_{O_2} = 0.21 atm) and (b) propagating region on the fracture surface for a bending sample with heat treatment in H_2/H_2O/Argon ($P_{O_2} = 8.8\times10^{-20}$ atm)

Since the elastic modulus decreased about 30% after the reduction treatment under $P_{O_2}= 10^{-22}$ atm, it is rather surprising to see the 37% improvement of the fracture toughness. In ideally brittle materials G_C is approximately equal to twice the surface energy. However, in real materials other factors may result in a higher elastic energy release rate value at the point of crack instability. Assuming the effect of defect formation through heat treatment on surface energy is insignificant, there has to be some microstructural reasons for the improved fracture toughness. The following discussion is presented to explain the increase in toughness upon heat treatment in reducing atmospheres based on the observations of the fracture surfaces.

A comparison of the fracture surfaces of the samples heat treated in air versus those heat treated in the $P_{O_2} = 8.8\times10^{-20}$ atm, revealed that in addition to the crack initiation differences, the fracture surface roughness was affected significantly by the environment. Consistent with the observations made for the Brazilian disc samples, the bending sample heat treated in the reduced atmosphere (Fig. 26b) exhibited a rougher fracture surface than the sample heat treated in air (Fig. 26a).

Crack deflection is known to increase the fracture toughness[43,44]. There are two types of crack deflection processes, these are tilt and twist. Both tilt and twist effects for the $P_{O_2} < 10^{-19}$ atm reduced samples come from the pre-existing micro-cracks. This concept is schematically shown in Fig. 27. In this figure, the loading direction (σ_{app}) is defined as the y- direction, consistent with Fig. 19. The tilt process (Fig. 27a) gives the roughness level along the primary

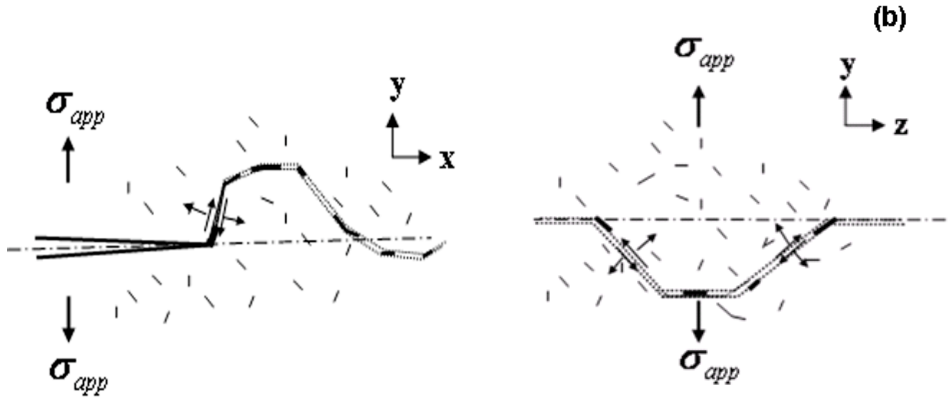

Figure 27. Schematics of fracture deflection process for the sample with pre-existing microcracks: (a) tilt mechanism and (b) twist mechanism. The dotted line represents the predicted fracture contour on the fracture surface. The dashed lines present the fracture surface without deflection process. The solid line segments represent the pre-existing microcracks and the ones that assist deflection process are thickened.

crack propagation direction, i.e. the x-direction, and the twist (Fig. 27b) explains the roughness along the z-direction. In this case, the roughness level on the fracture surface does not correlate directly with the distribution of the micro-cracks shown in Fig. 18. The overall roughness represents the probability of the primary crack front meeting the micro-cracks. The fact that the roughness level for the fracture surface of the samples heat treated in low P_{O_2} (shown in Fig. 26b) is much greater than the grain size level confirms these mechanisms. Therefore, during the loading process, the propagating crack front is anticipated to be deflected by the pre-existing microcracks resulting in an improved toughness.

Further observations of the fracture surface of a Brazilian disc sample heat treated under H_2/H_2O ($P_{O_2}=1.5\times10^{-20}$ atm) with $K_{53C}=1.39$ MPa•m$^{1/2}$ revealed the presence of multiple secondary cracks (marked with arrows in Fig. 28a). As shown in a higher magnification image of one of the secondary cracks (Fig. 28b), these secondary cracks actually were extended to the fracture surface after the primary crack had passed through, as evidenced by the continuity of the river marks.

The possible toughening mechanism is through micro-crack formation and extension, which has been discussed in detail in literature[45,46,47,48]. In samples heat treated at low oxygen partial pressure values the strain energy is released not only by the propagation of the main crack, but also by the extension of the pre-existing micro-cracks. In this case, the pre-existing micro-cracks with favorable orientations in the heavily stressed frontal process zone (ahead of

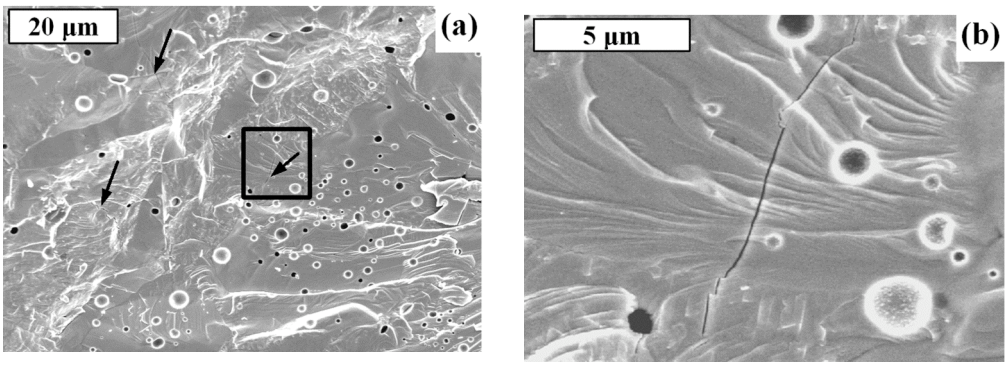

Figure 28. SEM images of the Brazilian disc sample heat treated under H_2/H_2O (P_{O_2} = 1.5×10^{-20} atm) with K_{IC}=1.39 MPa•m$^{1/2}$. The secondary cracks are marked with arrows in (a); (b) is the higher magnification image of the boxed area in (a).

the crack tip) are suggested to extend under the applied load. The extension of micro-cracks increases the material compliance and redistributes the near-tip stresses. Therefore, the critical strain energy release rate is increased[45]. In addition, we have demonstrated the fact (see Fig. 28) that upon crack propagation the unloading process in the wake of the main crack also caused the extension of the pre-existing micro-cracks onto the fracture surface. This phenomenon further contributes to the increase in the fracture toughness.

The interaction between pores and propagating cracks was also evaluated using a quantitative metallography analysis method for Brazilian disc samples. The pore area densities on the polished surfaces and the fracture surfaces were measured for samples heat treated under different conditions. Images from six different areas were measured for each type of surface. The pore area fraction calculated on the polished surfaces, i.e., ~6%, was consistent with the density of the material. Since the pore-crack interaction may be size dependent the calculations were conducted also for the pores with sizes less than 2.5 µm.

The results of the measurements are shown in Table 8. The air treated samples showed a higher area density on the fracture surface than on the polished surface, particularly for the smaller pores, indicating that the crack was attracted to the pores. However, the results for the H_2/H_2O (P_{O_2}=4.5×10^{-22} atm) treated sample suggest that the crack does not interact with fine pores and may be avoiding the larger ones. Based on this analysis, the pore-crack interaction is not responsible for the higher toughness of the samples heat treated in a reduced atmosphere.

Table 8. Pore-Crack Interaction for Brazilian Disc Test Samples

	Heat Treatment Condition	Surface Condition	Average Pore Area Density on Six Positions, %
All pores	Air (P_{O_2}=0.21 atm)	Polished	5.2±0.6
		Fractured	6.2±0.4
	H_2/H_2O ($P_{O_2}=4.5\times10^{-22}$ atm)	Polished	6.3±1.1
		Fractured	5.3±1.1
Fine pores (2.5-0.5 μm)	Air (P_{O_2}=0.21 atm)	Polished	2.9±0.4
		Fractured	3.8±0.5
	H_2/H_2O ($P_{O_2}=4.5\times10^{-22}$ atm)	Polished	2.1±0.2
		Fractured	2.2±0.3

In summary, for the samples heat treated under very low P_{O_2}, it is clear that pre-existing micro-cracks significantly decrease the flexural strength because of the larger and sharper defects. However, crack initiation is not important in measuring fracture toughness using pre-cracked samples and the results are controlled by the crack propagation process. The increase in the fracture toughness in low P_{O_2} atmosphere is associated with the micro-crack toughening and the crack deflection mechanisms.

ELECTROCHEMICAL PERFORMANCE

De-convolution of Electrical Impedance Spectra: A New Measurement Model

We were able to successfully apply a measurement model technique developed by Orazem *et. al*.[49] to electrical impedance spectroscopy (EIS) data taken from 950 °C sintered LSM on YSZ. A complex nonlinear least-squares (CNLS) regression technique was used to model the data and identify portions of the data which are Kramers-Kronig inconsistent. The model used consisted of a series resistance and six Voigt elements connected in series. As with most impedance data, a high-frequency artifact corrupted the high frequency data, limiting the frequency range of useful data. The models attained produced a good fit visually and the data values lied primarily within calculated 95 % confidence intervals (the dashed lines shown in Fig. 29). It was found that the commonly used practice of truncating the data at the Z_r axis left KK inconsistent data in the data set. To avoid inconsistent data, several data points with negative imaginary impedance had to be removed. The consistency of the data was improved by fitting the high-frequency portion of the data (which was shown to be inductive in nature) to $Z_j = j\omega L$ and subtracting the result from the raw data over the entire frequency range. Performing this operation increased the amount of usable data in the high-frequency regime by an order of magnitude as indicated by the arrows in Fig. 29(b). Performing this correction was necessary for the analysis of fast occurring electrochemical processes (e.g., charge transfer).

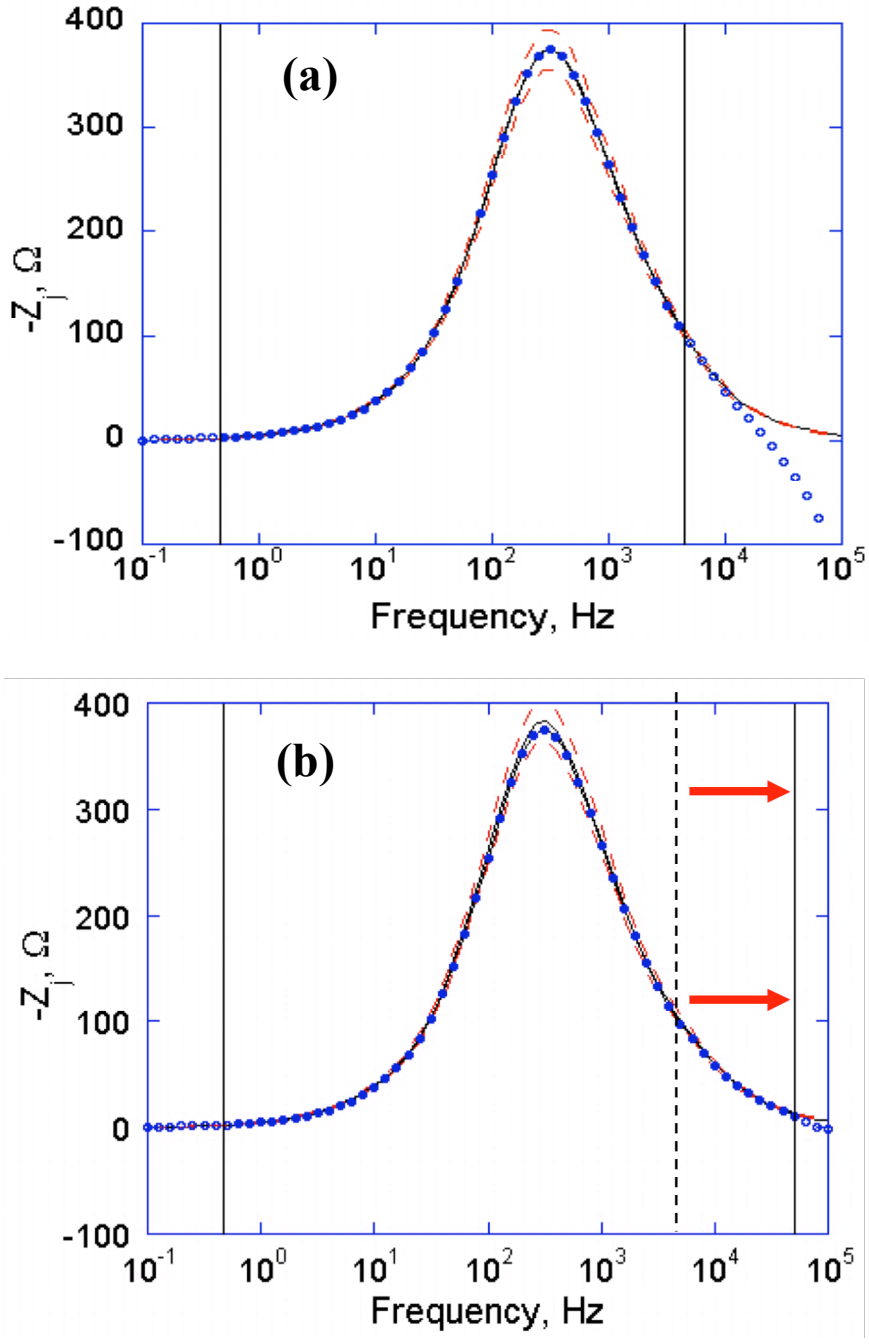

Figure 29. EIS data and model including 95% confidence interval for LSM on YSZ measured at 900 °C in imaginary impedance vs. frequency format. Model fit performed for (a) raw and (b) high-frequency corrected data. Arrows in (b) indicate the increase in the range of useable data

De-convolution of Electrical Impedance Spectra for LSM and LSCF

For an electronic conducting cathode, such as LSM, the overall sequence of steps (but not the specific mechanistic steps) defining the cathodic reaction is generally agreed on. The sequence begins with the arrival of O_2 molecules that have diffused through the porous cathode to the vicinity of the electrolyte. At some point after this diffusion, the molecules are adsorbed (dissociatively or as complete molecules) on the surface of the LSM. These adsorbed atoms now diffuse on the surface of the electrode towards the triple phase boundary, the area where the cathode, electrolyte and gas phase meet. At the same time, electrons (or holes) travel through the cathode, while oxygen vacancies travel through the electrolyte. For an electronic conducting cathode, the oxygen species are restricted from the bulk of the electrode, the oxygen vacancies are limited to the electrolyte, and the electronic species (electrons and holes) are limited to the cathode. For the complete cathodic reaction to occur, all of these species must come together; therefore, the cathodic reaction is limited to the TPB. The complete oxygen exchange reaction occurring at the TPB can be divided into charge transfer and ionic combination sub-reactions as indicated below[1,50]:

Oxygen exchange: $$O_{ads} + 2e' + V_O^{\bullet\bullet} \rightarrow O_O^{\times} \quad (40a)$$

Charge transfer: $$O_{ads} + 2e' \rightarrow O''_{ads} \quad (40b)$$

Ion combination: $$O''_{ads} + V_O^{\bullet\bullet} \rightarrow O_O^{\times} \quad (40c)$$

Figure 30 shows Nyquist and -Z" vs. frequency plots of symmetric LSM samples sintered at 1100 °C for 1 h and measured at various temperatures in air. The peaks and changes in slope of the -Z" vs. frequency plot indicate the characteristic frequencies of the significant steps of the cathodic reaction. The 900 °C arc in Fig. 30(a) is almost semicircular, having slight asymmetry. This geometry indicates that there is one large resistance process enveloping another smaller resistance high frequency process. At the lower temperatures displayed in Fig. 30(b), two other processes are apparent which are attributed to oxygen vacancy diffusion through the bulk and grain boundaries of the electrolyte[51]. These processes are smaller in magnitude than the cathode processes, but at lower temperatures, the cathode processes are not seen in the profile. At higher

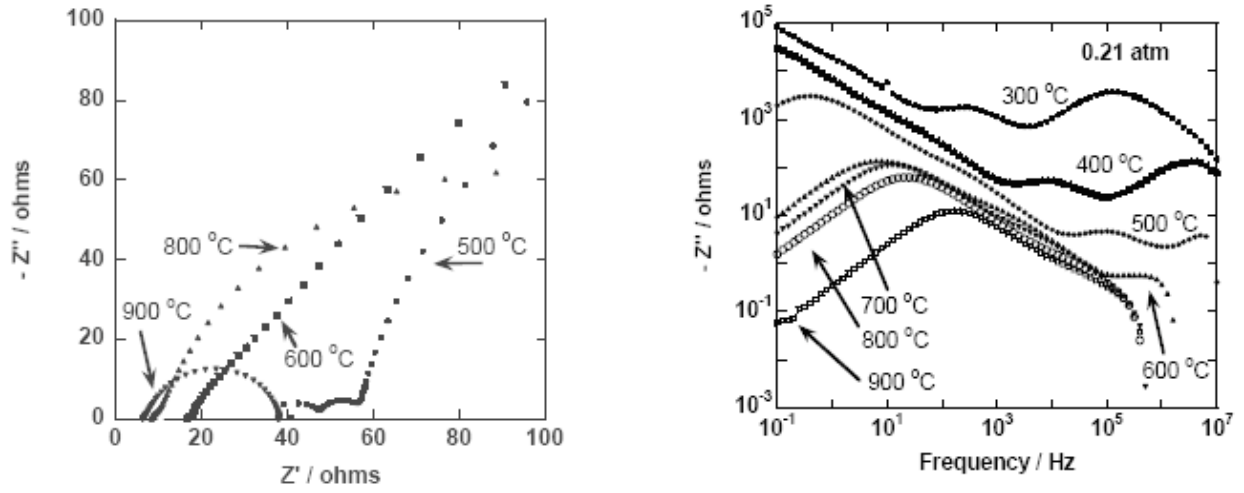

Figure 30. Impedance response of LSM on YSZ in air with temperature as a parameter. (a) Nyquist plot, (b) magnitude of imaginary impedance as a function of frequency.

temperatures, the electrolyte processes have very small resistance and are overwhelmed by the cathodic processes and inductive artifacts.

Each of the impedance profiles included in Fig. 30 were separated by a subtraction technique into the various contributions. Because the primary focus of this work is identification of time constants of the individual reaction steps, use of constant phase elements in the place of the capacitors in the Voigt elements of the model is appropriate. Modeling with pure capacitors is limited in that multiple Voigt elements may be required to model a single process step if the behavior is inhomogeneous; otherwise, compromises may have to be made to match only a selected portion of the curve. Also, if the homogeneity changes over the range of temperatures measured, the depression angle of the arc may change, resulting in a non-Arrhenius dependence of resistance and time constant on temperature.

Figure 31 illustrates the separation of the 500 °C measurement of symmetric LSM on YSZ cells sintered at 1100 °C into four contributing electrochemical processes. Each of the indicated electrochemical processes is modeled by a single R–CPE Voigt element. This separation was repeated at all measurement temperatures for the sample.

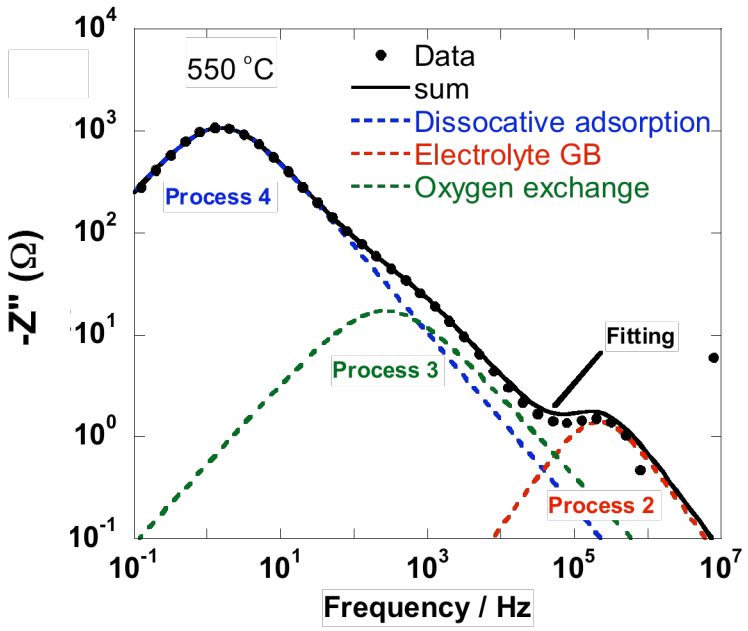

Figure 31. Separation of an impedance profile into various individually contributing processes

Evaluation of Time Constants for Electrode Processes: LSM on YSZ

Figure 32 shows the Arrhenius dependence of polarization resistance and time constant for the LSM 1100 °C, 1 h sintered sample. The time constant, τ, is calculated as

$$\tau = (RQ)^{1/\alpha} \tag{41}$$

where R is the polarization resistance, Q and α are the non-exponential and exponential terms of the constant phase element, respectively. The activation energy, E_a, for the polarization resistances of the individual reactions can be calculated as

$$R = R_0 \mathbf{exp}(E_a/kT) \tag{42}$$

where R_o is a constant, k is Boltzmann's constant, and T is temperature.

Examination of Fig. 32(a) reveals that there is some change in slope in the high temperature region of process 4. This is an indication that the changes in slope in the high temperature regime were due to either changes in the homogeneity of the dominant electrochemical process step, or a contribution from a different electrochemical process with a

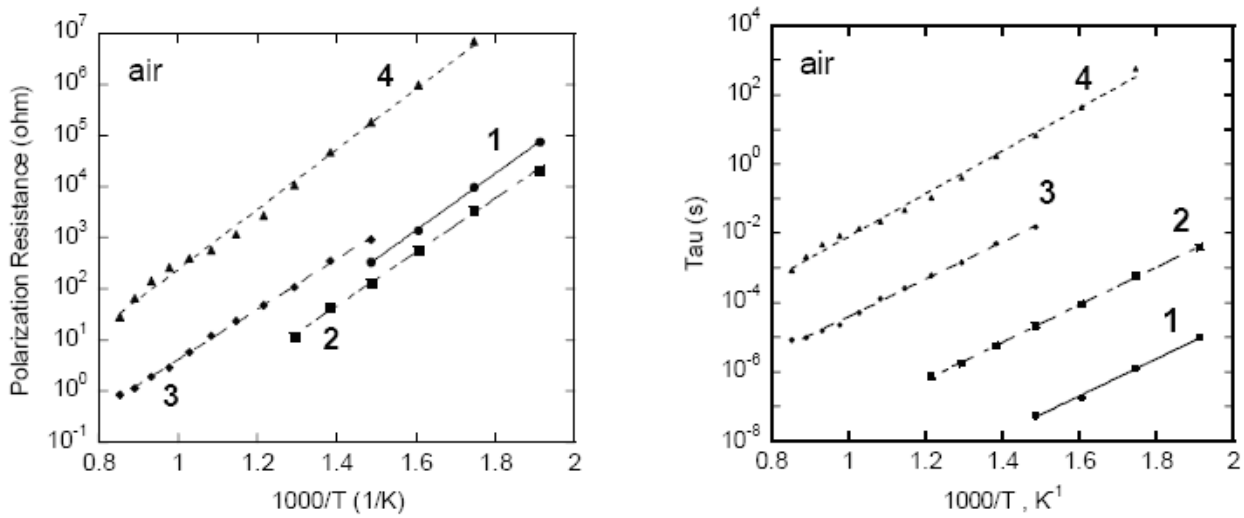

Figure 32. Temperature dependence of the identified electrode processes for LSM on YSZ sintered at 1100 °C for 1 h in air. The numbers indicate the process step number, which are given in Table 9; (a) polarization resistance, (b) time constant.

different activation energy. Figure 32(b) indicates a somewhat smoother profile in the same region for the same process. This supports the former of the two possibilities, that the effect of varying depression angles on the resistance or time constant would be minimized in the time constant calculation. Knowledge of the Arrhenius dependence of the polarization resistance and time constant of the individual electrochemical process steps is all the information needed to generate the impedance profile as a function of only temperature. The polarization resistance and time constant activation energies are presented in Table 9.

Figure 33 shows the influence of P_{O_2} on the various electrochemical processes occurring at 900 °C. Oxygen partial pressures ranging from 0.21 to 1×10^{-6} atm were created by mixing air with argon. The figure indicates that a second process in the low frequency regime gains significant magnitude at low P_{O_2} values. The process is first resolvable at 0.001 atm and grows

Table 9. Select elementary steps of the cathodic reaction in LSM on YSZ.

Step #	Process Identity	"x" in $R \propto (P_{O_2})^x$	E_a (eV)	τ (s) @ 800 °C
1	Ionic diffusion through electrolyte bulk	0.00	1.10	-
2	Ionic diffusion through electrolyte grain boundary	0.00	1.04	-
3	Exchange of oxygen between cathode and YSZ	0.00	0.97	8.50×10^{-5}
4	Dissociation & surface diffusion of oxygen species	-0.15	1.17	0.18
5	Gas diffusion through porous cathode	-1.1	0.00	6.00

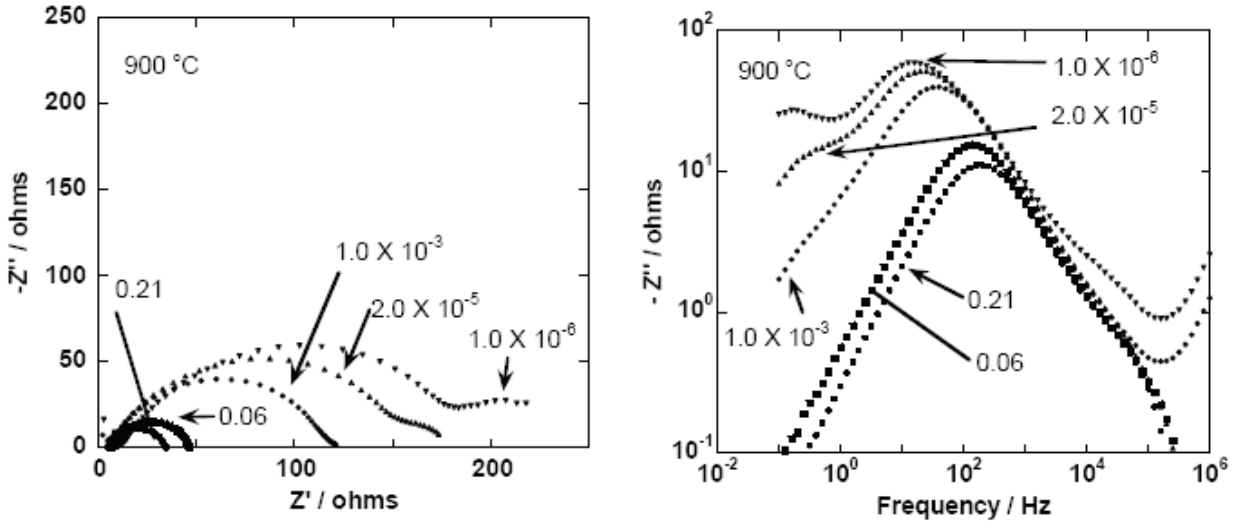

Figure 33. Impedance response of LSM on YSZ at 900 °C with oxygen partial pressure (atm) as a parameter. (a) Nyquist plot, (b) magnitude of imaginary impedance as a function of frequency.

as P_{O_2} is further reduced. The dependence of polarization resistance on P_{O_2} is displayed in Fig. 34. The high frequency section of Fig. 33(b) shows an increase in imaginary impedance for the lower P_{O_2} measurements. It appears that the increase in imaginary impedance above 10^5 Hz is an experimental artifact due to induction and not the result of some new high frequency process that is not present at the higher P_{O_2}'s.

A comparison of Figs. 34(a) and (b) shows that the low frequency process has a significantly stronger dependence on P_{O_2} than the other processes. The dependence of polarization resistance can be expressed as $R \propto (P_{O_2})^x$; where the exponential value, x, is equal to the slope of the line in Fig. 34. Values of x are indicated in Table 9. The strong dependence of this process on P_{O_2} indicates that it is very closely related to oxygen diffusion. Because impedance spectroscopy is an electrochemical measurement technique, the diffusion of gas molecules can't be registered until they are converted into a species that can participate in the electrochemical reaction[52]. A rapidly adsorbing surface, which permits an oxygen flux equal to the flow of gas through the open pores, would produce such an effect.

The lowest frequency arc (process 5) in the lowest partial pressure regime is due to a process limited by the bulk diffusion of oxygen molecules to the adsorbing surface. The two processes (process 1 and 2) which are present in the high frequency regime and at low temperatures, become hidden at higher temperatures. These processes are likely due to the

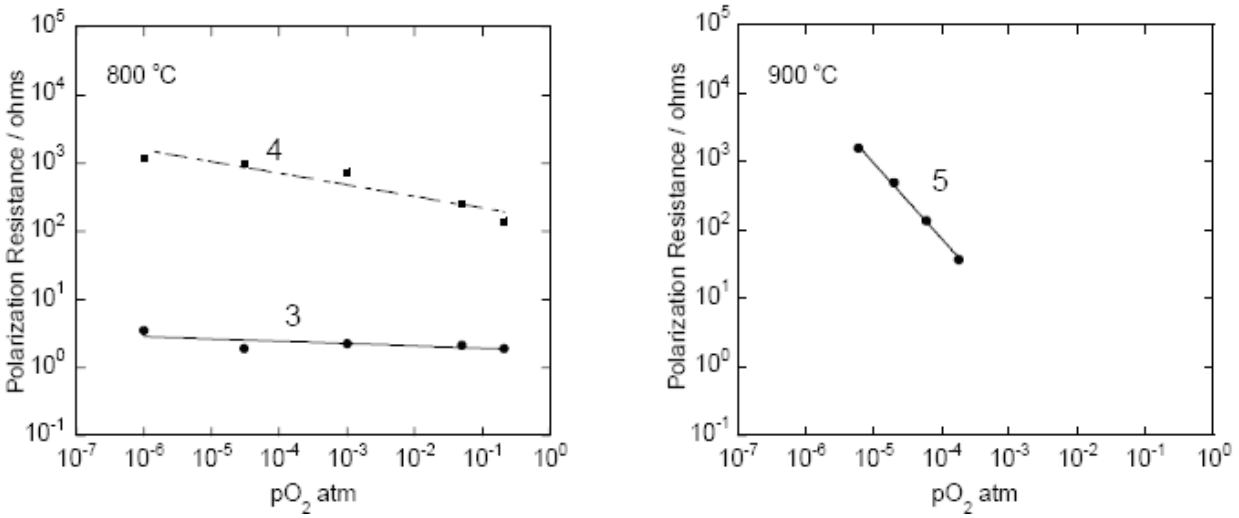

Figure 34. Dependence of cathodic polarization resistances in LSM/YSZ sintered at 1100 °C on P_{O_2}. The numbers indicate the process steps given in Table 9. (a) at 800 °C, (b) at 900 °C.

electrolyte bulk and grain boundary, a conclusion supported by their determined activation energies. This leaves two as yet unidentified processes, which can be attributed to the cathodic reaction. One of these processes has much smaller impedance and is located in the high frequency regime, and the other is located in the lower frequency regime and has much larger impedance, greatly influencing the overall shape of the Nyquist plot at high temperatures. An oxygen exchange reaction, involving charge transfer located at the TPB, would be expected to be a rather fast process with weak dependence on P_{O_2}. Figure 34(a) indicates that process 3 is nearly independent of P_{O_2}, while process 4 is has an exponential dependence of –0.15. This indicates that process 3 is due to oxygen exchange at the TPB. The stronger dependence of process 4 on P_{O_2} indicates this process is closely related to molecular oxygen. Adsorption, dissociation, and surface diffusion are all possibilities for the identity of process 4, which has a stronger dependence on temperature and P_{O_2} than the oxygen exchange reaction. The identities of the contributing processes are summarized in Table 9.

Figure 35(a) shows the imaginary impedance dependence of a 1200 °C, 1 h annealed sample. We observe an increase in the impedance of the gas diffusion related process by more than an order of magnitude. The calculated time constant had a value of 5.3 s for $P_{O_2} = 2 \times 10^{-5}$ atm, which is similar to the time constant calculated for the 1100 °C sintered sample. There is a shift in the peak frequency of the higher P_{O_2} measurements. The increase in the impedance

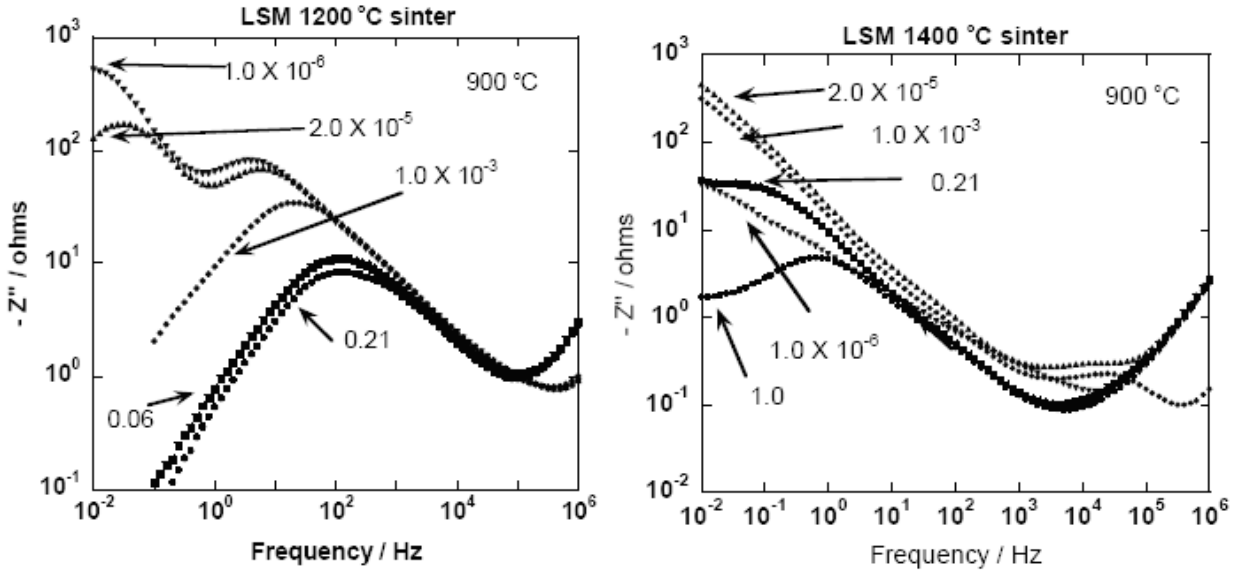

Figure 35. Magnitude of imaginary resistance as a function of frequency with P_{O_2} (atm) as a parameter. (a) sintered at 1200 °C for 1 h, (b) sintered at 1400 °C for 1 h.

magnitude of the diffusion related peak indicates that gas molecules are being inhibited as they attempt to reach the cathode surface and participate in the cathodic reaction. Cathode coarsening would block the gas transport and cause this effect.

Figure 35(b) shows the imaginary impedance vs. frequency behavior of a 1400 °C annealed sample. For this sample, there is no peak between 10 and 10^5 Hz. This indicates that the oxygen exchange reaction is not occurring. Additionally, the dissociation related arc is not occurring in the expected frequency range. It has been shown by several authors that lanthanum zirconate, an insulating oxide, can form as a reaction product between LSM and YSZ at these temperatures. This insulating phase, if formed in a complete layer, would block the TPB reaction and produce the result that is displayed in the figure. Once again inductive artifacts are present at the highest frequencies and cause an increase in imaginary impedance magnitude above 10^5 Hz in some of the measurements.

Figure 36 shows the microstructure of LSM on YSZ samples annealed for one hour at various temperatures. At 950 °C, the particles are still relatively jagged and maintain their individual nature. By 1100 °C, some coarsening has occurred. More significantly, the inter-particle contacts are going from point-to-point to face-to-face. This change should ensure efficient transport of electrochemical species through the cathode microstructure. This is the optimally sintered microstructure. By 1300 °C, the particles are losing their individual nature,

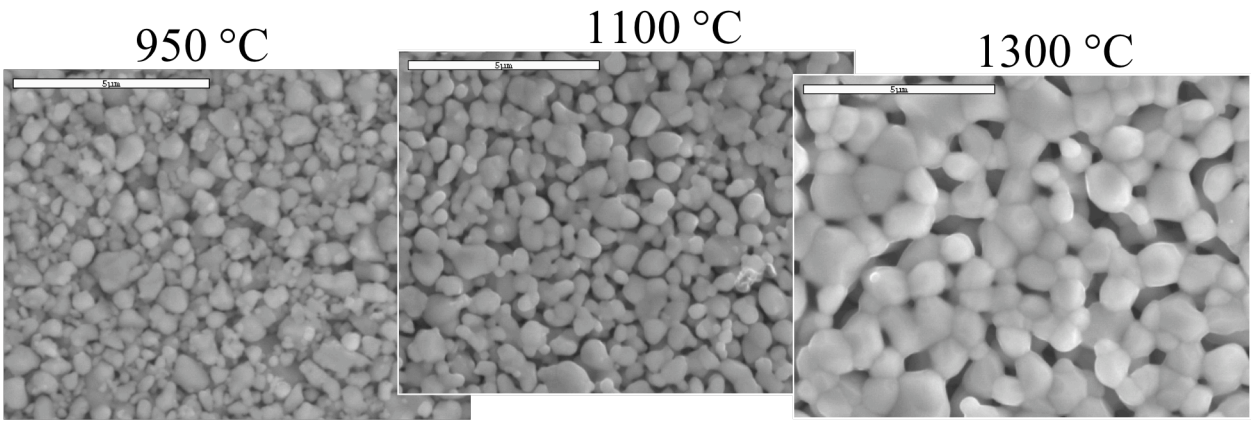

Figure 36. SEM images of LSM microstructure at various sintering temperatures. 950 °C (a), 1100 °C (b), and 1300 °C (c).

coarsening has become severe, and the open channels for gas passage are beginning to be blocked. This microstructure is over-annealed. However, this analysis is only qualitative, and for any mechanistic determination, a quantitative analysis of the cathode microstructure is necessary.

Under support from the Department of Energy High Temperature Electrochemistry Center (DOE-HiTEC) at the University of Florida (Contract #: DE-ACO5-76RL01830), further analysis of the LSM on YSZ samples, using a focused ion beam combined with simultaneous SEM (FIB/SEM) was performed. Figure 37 shows the microstructure of LSM on YSZ sintered for 1 h at 1100, 1200, and 1400 °C. There is increased grain coarsening at 1200 °C, as compared to 1100 °C and the LSM layer is dense at 1400 °C. Details of the technique and the results of the quantification of the microstructure are given in the literature[53,54]. Some of the results are

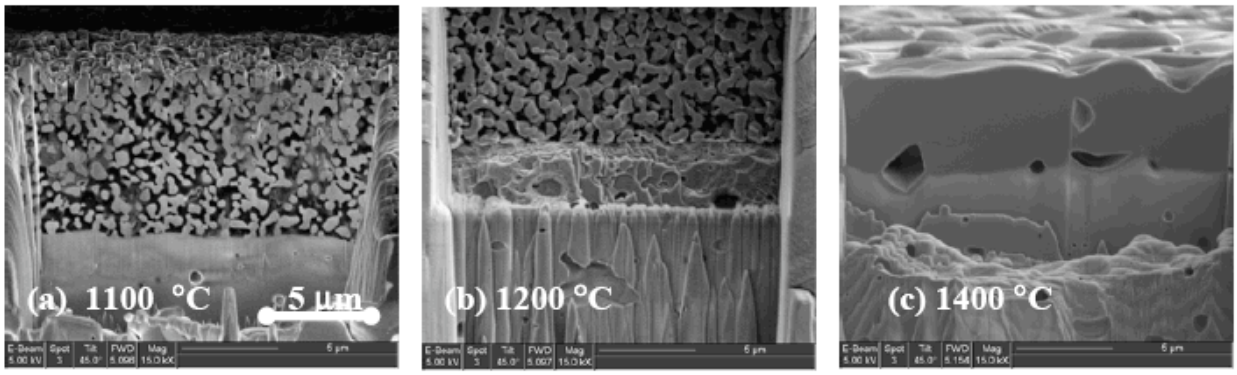

Figure 37. (a-c) Cross-sectional SEM images of LSM on YSZ with 1 h anneals at various sintering temperatures.

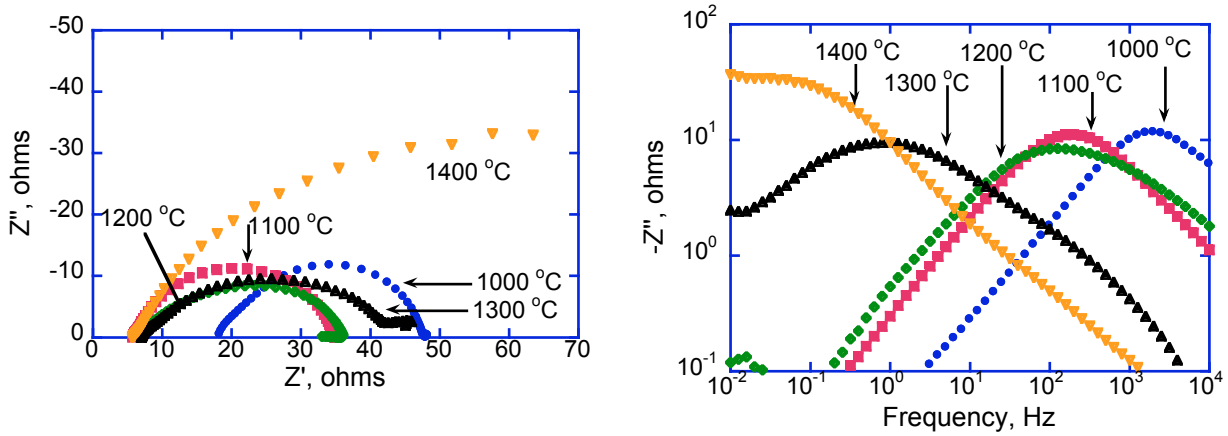

Figure 38. Nyquist (a) and imaginary impedance vs. frequency (b) plots measured at 900 °C in air for LSM on YSZ sintered at various temperatures for 1 h.

presented here to make the analysis of the effect of microstructure more quantitative and are discussed in greater detail below.

Figure 38 shows the influence of sintering temperature on impedance spectra. Figure 38(a) shows the data in a Nyquist plot, while Fig. 38(b) shows the data in the imaginary impedance vs. frequency format. Because time constants are inversely proportional to peak frequency, we can extract information about the influence of sintering temperature on time constants of the highest magnitude resistance process by examining the shift in peak frequency.

Looking first at Fig. 38(a), we see that the high-frequency intercept for all the sintering temperatures except 1000 °C have similar values. The high value for the 1000 °C sintered sample is due to incomplete adhesion between the cathode particles and/or between the cathode particles and the YSZ electrolyte. This poor adhesion provides for inefficient conduction, resulting in the increased magnitude of the intercept seen in Fig. 38(a). Figure 38(b) shows a clear trend of decreasing peak frequency as sintering temperature is increased. This trend indicates an increasing time constant as sintering temperature is increased. The coarsening of the cathode reduces the triple phase boundary length per unit area and decreases available surface area for adsorption to occur. The result is clearly that the electrochemical process steps which must occur for the cathodic reaction to take place are slowed by the overly coarse microstructure. There is only minimal change in the time constant of the overall reaction between 1100 °C and 1200 °C, indicating that coarsening is not advanced in this temperature range. Turning our

attention once again to the 1000 °C sintered sample, we see that the peak frequency of the overall reaction has increased as compared to the 1100 °C sintered sample.

Evaluation of Time Constants for Electrode Processes: LSCF on YSZ

Significant differences were found in the electrode process occurring in the LSCF/YSZ electrode/electrolyte system compared to the LSM/YSZ system. For an LSCF sample sintered at 950 °C for 1 h, the impedance results at various temperatures in air and at 700 °C in various atmospheric conditions are shown in Figs. 39 and 40, respectively. The incomplete semicircles in the high frequency end of Figs. 39(a) and 40(a) are due to an inductance subtracted from the raw data. Figure 39(b) displays multiple processes occurring, with electrolyte related processes being discernable only at low temperatures. At the higher temperatures under which the cathodic processes dominate, there is a large peak with at least two distinct changes of slope. This is a direct indication of multiple cathodic process steps occurring as evidenced by the asymmetrical nature of the cathodic arc in Fig. 39(a).

Figure 40(a), shows an intermediate frequency semicircle with an additional low frequency arc for $P_{O_2} \leq 0.001$ atm. The shifting in the real impedance intercept is due to the mixed ionic conducting nature of LSCF. As less oxygen is available to convert into charge

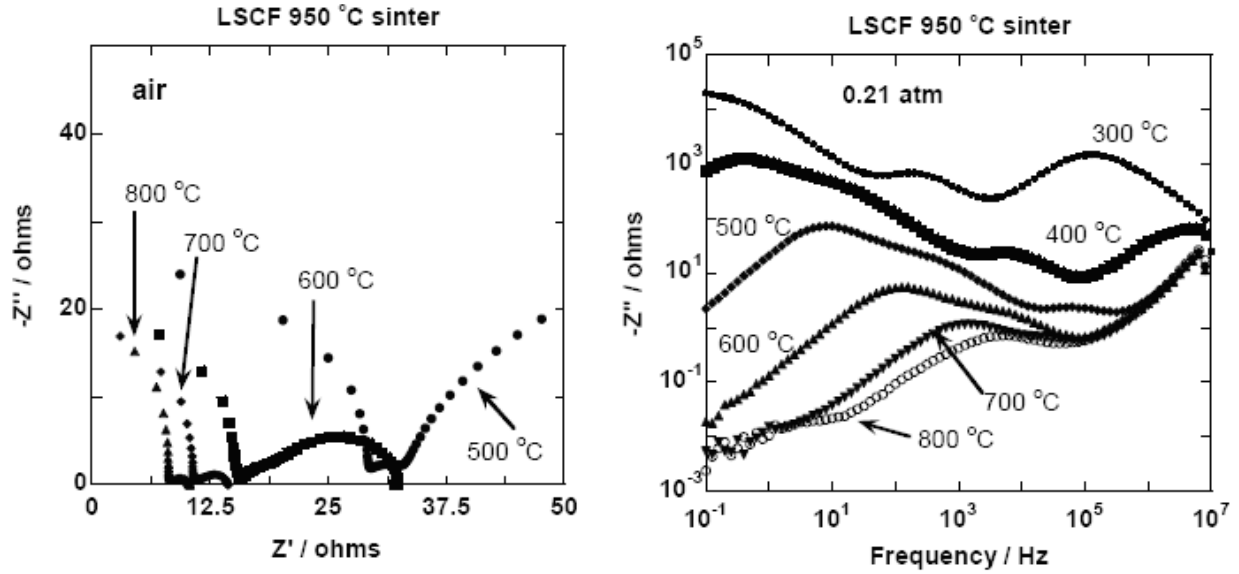

Figure 39. Impedance response of LSCF on YSZ sintered at 950 °C in air with temperature as a parameter. (a) Nyquist plot, (b) magnitude of imaginary impedance as a function of frequency.

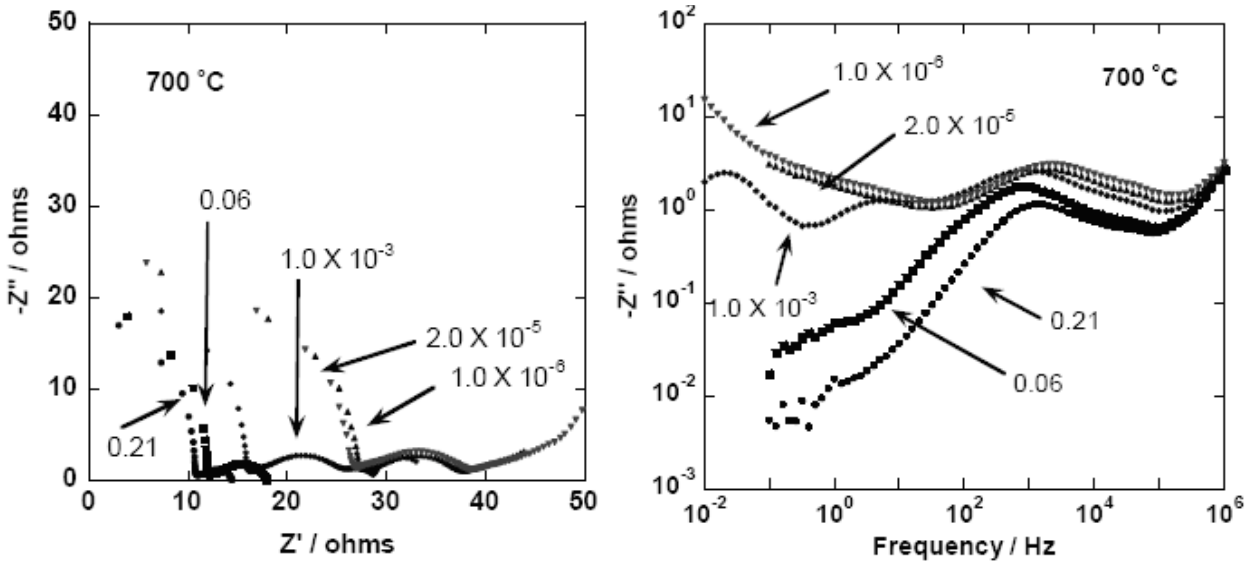

Figure 40. Impedance response of LSCF on YSZ sintered at 950 °C and measured at 700 °C in various P_{O_2}'s (atm): (a) Nyquist plot, (b) magnitude of imaginary impedance vs. frequency.

carriers, ionic conduction in the cathode is able to account for less of the total conduction of carriers to and from the electrolyte and the high frequency intercept with the real impedance axis increases. Comparison of the 0.001 atm imaginary impedance plot for LSCF displayed in Fig. 40(b) with Fig. 33(b) illustrates some key differences between the two materials systems.

First, the gas diffusion related semicircle is easily resolved at 0.001 atm in the LSCF, while for the LSM system, this process was barely resolvable at this partial pressure. This effect is likely due to the decreased resistance seen for the LSCF sample. The gas semicircle is likely to have been just overshadowed by the other polarization resistances in LSM until its polarization resistance magnitude is comparable to the others. Secondly, three cathodic processes of similar imaginary impedance magnitude are clear in the LSCF sample. This more complicated behavior is due to the MIEC nature of LSCF.

The time constants for LSCF sintered at 950 °C and 1 h in air and 0.001 atm P_{O_2} are displayed in Fig. 41. Four electrochemical contributions were required to fit the profile obtained in air and the Arrhenius dependence of these four contributions is shown in Fig. 41(a). Of these four processes, processes 1 and 2 are due to the electrolyte bulk and grain boundary, respectively. Moreover, within experimental error, they are identical to those obtained in the study of LSM on YSZ, Table 9. The remaining two processes, 3 and 4, are cathodic processes.

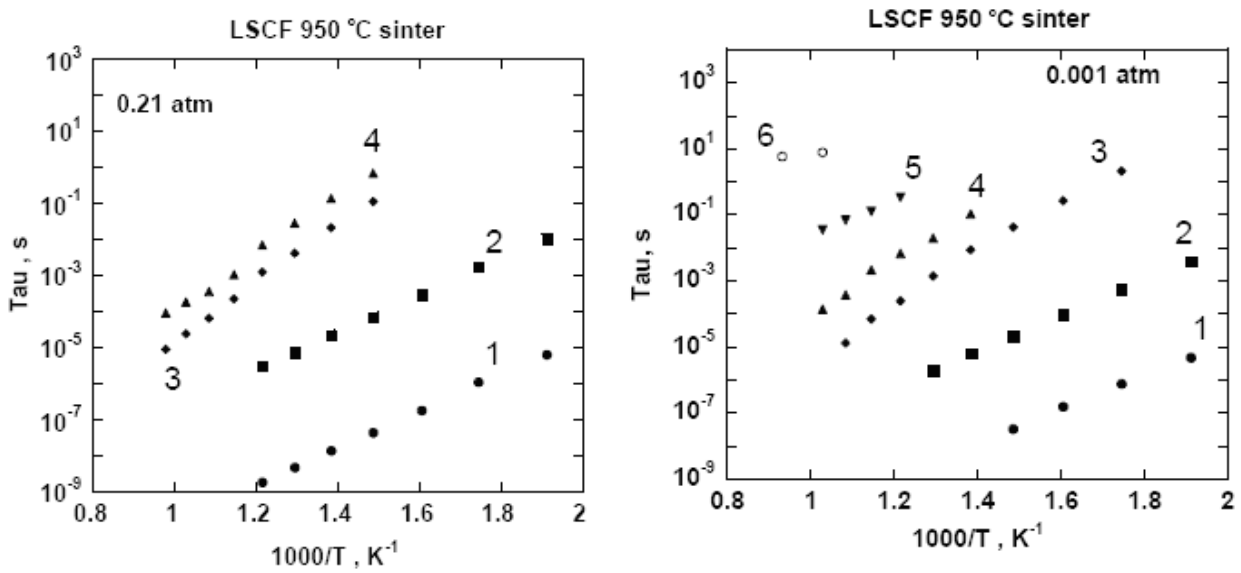

Figure 41. Temperature dependence of the identified electrode processes for LSCF on YSZ sintered at 950 °C for 1 h and tested (a) in air and (b) at 0.001 atm.. The numbers indicate the process step number given in Table 10.

Comparison of the slope of these processes with the cathodic processes occurring in LSM (processes 3 and 4 in Fig. 32(a)) reveals that the cathodic processes in LSCF have a stronger dependence on temperature than the cathodic processes of LSM in air. At 0.001 atm, electrochemical processes not seen in air are exposed. Indeed, six electrochemical contributions were necessary to fit the complex impedance profile obtained at 0.001 atm. Fig. 41(b) shows the temperature dependence of these six contributions. Once again, processes 1 and 2 are due to the electrolyte bulk and grain boundary, respectively. Processes 3 and 4 were also seen in LSCF in air as shown in Fig. 41(a). The low frequency process, 6, is essentially independent of temperature, and is due to the gas diffusion related process. In addition, it has the same P_{O_2} dependence, activation energy, E_a, and time constant, τ, found in the LSM on YSZ study, which we also assigned to gas diffusion. The other extra cathodic process, process 5, has a weaker temperature dependence than LSCF processes 3 and 4, but similar dependence as the cathodic processes, 3 and 4, occurring in LSM. The time constant and other relevant values for the multiple LSCF processes are displayed in Table 10.

Table 10. Select elementary steps of the cathodic reaction in LSCF on YSZ.

Step #	Process Identity	"x" in $R \propto (P_{O_2})^x$	E_a (eV)	τ (s) at 700 °C
1	Ionic diffusion through electrolyte bulk	0.0	1.10	-
2	Ionic diffusion through electrolyte grain boundary	0.0	1.00	-
3	Cathodic process	-0.049	1.34	8.80×10^{-6}
4	Cathodic process	-0.041	1.08	1.40×10^{-4}
5	Cathodic process	-0.20	1.12	0.036
6	Gas diffusion through porous cathode	-1.1	0.00	8.00

Effect of Microstructure on Electrode Polarization

Using the quantitative microstructural information obtained under the support of the Department of Energy High Temperature Electrochemistry Center (DOE-HiTEC) at the University of Florida (Contract #: DE-ACO5-76RL01830) and our deconvoluted impedance data for LSM on YSZ (previous section), the relationship between electrode microstructure and electrode polarization was investigated. Figure 42 relates the electrochemical performance caused by varying sintering temperature to the microstructural changes by showing the influence of area normalized TPB length on charge transfer resistance R_{ct} and the influence of volume normalized pore surface area on adsorption resistance R_a. Focusing first on charge transfer, we see that the charge transfer resistance increases as triple phase boundary length decreases.

Curve fitting of the data indicates that there is a power-law dependence of charge transfer R_{ct} on L_{TPB} of the form:

$$R_{ct} = 2.93(L_{TPB})^{-3.5} \tag{43}$$

A power law dependence can be predicted if we consider the kinetic behavior of reactions. For a given chemical reaction, the rate equation can be written as

$$\nu = k[A]^a[B]^b \tag{44}$$

After adsorption of gas molecules on the surface of the cathode, a charge transfer reaction occurs at the cathode/electrolyte interface. Let us assume, for now, that adsorption and charge transfer occur according to the following, respective, reactions:

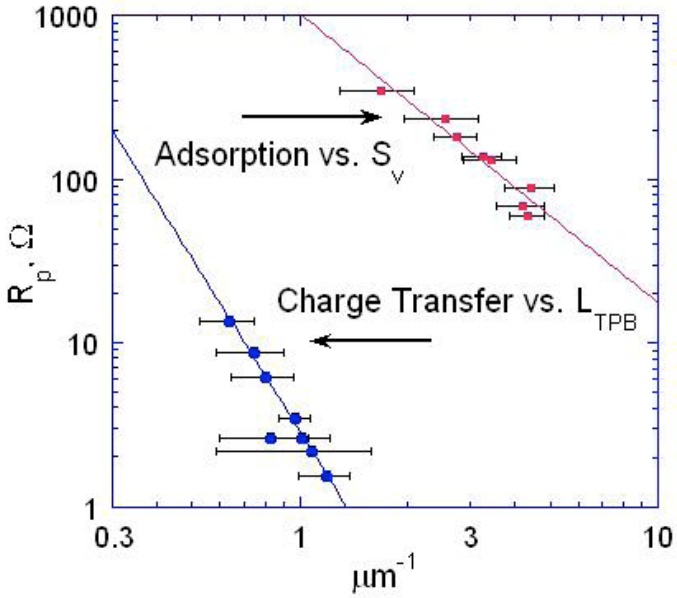

Figure 42. Relation of charge transfer and adsorption polarization resistance for LSM on YSZ in air at 800 °C to microstructural quantities.

$$O_2 + s \rightarrow O_{2,ads} \tag{45}$$

$$\tfrac{1}{2}O_{2,ads} + 2e' + V_O^{\bullet\bullet} \rightarrow O_O^{\times} + s \tag{46}$$

The rate of the charge transfer reaction indicates how quickly charged species are being transferred across the cathode/electrolyte interface. This exchange of charged species determines the exchange current, I_0. If the individual species of the charge transfer reaction are treated as reactants and products, then the exchange current can be expressed as

$$I_0 = k_f\left[e'\right]^m\left[O_{2,ads}\right]^n\left[V_O^{\bullet\bullet}\right]^p - k_r\left[O_O^{\times}\right]^q\left[s\right] \tag{47}$$

where the forward and reverse rate constants, k_f and k_r, account for balance of units. In the Equation $[e']$, $[O_{2,\,ads}]$, $[V_o^{\bullet\bullet}]$, and $[s]$ are the concentration of electrons, adsorbed oxygen, oxygen vacancies, and surface sites on the cathode able to participate in the cathodic reaction, respectively. The second term on the right side of the equation describes the rate of the reverse reaction. For simplicity, we will assume this term can be neglected.

The interfacial reaction is impeded by a charge transfer resistance, R_{ct}, which under equilibrium conditions has been shown to be

$$R_{ct} = \frac{RT}{nFI_0} \tag{48}$$

where R is the gas constant, T, n, and F have their usual meaning. Substituting I_0 from Eq. (47) gives (at the TPB)

$$R_{ct} = \frac{RT}{nFk_f}\left[e'\right]_{\mathrm{TPB}}^{-m}\left[\mathrm{O}_{2,ads}\right]_{\mathrm{TPB}}^{-n}\left[\mathrm{V}_{\mathrm{O}}^{\bullet\bullet}\right]_{\mathrm{TPB}}^{-p} \tag{49}$$

where for LSM on YSZ, only the number of species in the vicinity of the triple phase boundary (TPB) can participate in the cathodic reaction. In order to relate the number of species in the vicinity of the TPB to the bulk concentration of species in their respective phases, we need to multiply the concentration of species by the TPB volume of their respective phase.

The number of the ith active species N_i, at the triple phase boundary, is given by:

$$N_i = [i]_{TPB} A_{TPB} L_{TPB} \tag{50}$$

where $[i]_{\mathrm{TPB}}$ is the concentration of the ith active species, L_{TPB} is the TPB length and A_{TPB} is the TPB area. Also, since the charge transfer reaction is confined to the TPB for LSM on YSZ, then A_{TPB} is a constant; independent of microstructural variables and determined solely by the participant species.

Substituting Eq. (50) into Eq. (49) yields:

$$R_{ct} = \frac{RT\left(A_{TPB}^{-(m+n+p)} N_{e',TPB}^{-m} N_{\mathrm{O}_{2,ads},TPB}^{-n} N_{\mathrm{V}_{\mathrm{O}}^{\bullet\bullet},TPB}^{-p}\right)}{nFk_f} L_{TPB}^{-(m+n+p)} = BL_{TPB}^{-(m+n+p)} \tag{51}$$

where B is a constant.

The exponential quantity (n+m+p) gives the reaction order dependence on L_{TPB}. In chemical reactions the reaction order can be given by the coefficients in the balanced chemical equation. If we assume that the charge transfer reaction is of the form of Eq. (51) and that the exponential terms, m, n, and p are given by the coefficients in Eq. (46), then a reaction order of -3.5 is predicted and $R_{ct} \propto L_{TPB}^{-3.5}$ which is exactly what was observed in Fig. 42.

A relationship between adsorption resistance, R_a, and volume normalized pore surface area is also established as shown in Fig. 42. The data was fit to a power-law relationship giving $R_a = 1025(S_V)^{-1.76}$. Because impedance spectroscopy is an electrochemical technique, it cannot detect the presence of adsorbed species unless they participate in the electrochemical reaction. If we assume that the charge transfer reaction, Eq. 46, is the rate limiting step then the species generated in the adsorption can only be detected after the charge transfer reaction occurs, i.e. the rate we detect. Therefore, generation of adsorbed species is limited by the rate of the charge transfer reaction. Every time adsorption (Eq. 45) occurs, an $O_{2,ads}$ is generated. For each $O_{2,ads}$ generated, however, the charge transfer reaction (Eq. 46) can occur twice. We can conclude that if the reaction is charge transfer limited, and adsorption does not occur dissociatively, the rate of the adsorption reaction is one half that of the charge transfer reaction. Hence, we expect the reaction order dependence of adsorption resistance on L_{TPB} to be smaller than -3.5 and in fact we find it to be $-1.76 \approx (n+m+p)/2$. Varying P_{O_2} and temperature will have an effect of changing the rate-limiting step and future work will investigate the influence of P_{O_2} and temperature on the determined reaction order.

CONCLUSION

Based on the fundamental laws of physics and thermodynamics we developed analytical models to predict the electrochemical performance of SOFCs, and thermo-mechanical and thermo-chemical stability of SOFC materials. These models were derived with minimal approximations (e.g., the defect concentrations in the ceramic lattice were assumed to be within the dilute limit) and due to their fundamental nature provide SOFC developers the necessary tools to select new materials and microstructures and predict their impact on SOFC performance and stability.

The models were developed to relate the concentration of point defects in common SOFC materials with the fluorite structure (YSZ, GDC, and ceria) to environment (oxygen partial pressure and temperature), SOFC operating conditions (load voltage and current in both steady state and transient conditions) for single layer and multilayer architectures.

The models were demonstrated to be self-consistent, in that by obtaining fundamental constants from a single experiment (e.g., equilibrium constant for oxygen-vacancy formation from thermogravimetry) we could use the same constant to model everything from conductivity to thermo-chemical expansion and elastic modulus, without modification or arbitrary fitting parameters. Further, the models and their predictions were experimentally verified to be correct.

The extensive body of work has resulted in 14 publications in scientific journals, ranging from the *Journal of the Electrochemical Society* to *Journal of Applied Physics*, as seen in Table 11. Some of the highlights of this work are:

- A simple analytical expression for the thermo-chemical expansion (both temperature and P_{O_2} effect) for YSZ and GDC was developed and validated. A solution was also obtained and validated for ceria but requires numerical methods to solve due to defect association effects.
- A simple analytical expression for the P_{O_2} effect on bulk elastic modulus was developed and validated for YSZ and GDC. A solution was also obtained and validated for ceria but requires numerical methods to solve due to defect association effects.
- The effect of P_{O_2} on the elastic modulus of polycrystalline YSZ, GDC, and ceria was experimentally demonstrated to be similar to that predicted from our models for the bulk elastic modulus.

- A model was developed to determine the P_{O_2}, and thus chemical stability, between SOFC constitutive layers under operating conditions.
- A complete solution for the electrochemical performance of SOFCs was developed. The model takes into account all the important factors contributing to the electrochemical performance of SOFCs, such as component (anode, electrolyte, cathode) thickness, thickness ratio, microstructure, gas composition, temperature material type and operating conditions (current density, P_{O_2} at the electrodes, overpotential) and does so with less fitting parameters than any other existing model.
- The SOFC electrochemical performance model was extended to transient (both power conditioning and air/fuel disruptions) operation. The model shows the effect SOFC layer thickness has on the transient time constants and its implications should be considered in SOFC design.
- A technique was developed to improve the quality of Electrochemical Impedance Spectroscopy (EIS) data and applied to de-convolute LSM and LSCF cathode impedance, into their various contributions, while simultaneously obtaining the time constant for each of the relevant processes.
- By analyzing this de-convoluted cathode impedance data and comparing it with quantified cathode microstructure data (from our DOE High Temperature Electrochemistry Center contract # DE-AC05-76RL01830) we were able to, for the first time ever, directly and quantitatively relate cathode polarization to specific microstructural features (triple phase boundary length and pore surface area).
- Finally, software modules for the analytical models were written in the computer languages, C++ and PHP capable of operating on a simple PC or incorporated into CFD (computational fluid dynamics) software used by SECA teams.

The models are directly relevant to SOFC developers both in optimizing their design with existing materials and in considering new materials and architectures to improve their design. While the appropriate materials constants were obtained and the models validated for fluorite based (electrolyte) materials, the models would have even more utility if the materials constants were obtained, and models validated for, perovskite based (cathode) materials. This would then complete the models and materials set necessary for developers to rationally design SOFCs.

Table 11. Scientific Publications submitted so far from this contract.

1. "Evaluation of the Relationship Between Cathode Microstructure and Electrochemical Behavior for SOFCs," J.R. Smith, A. Chen, D. Gostovic, D. Hickey, D. Kundinger, K.L. Duncan, R.T. DeHoff, K.S. Jones and E.D. Wachsman, *Solid State Ionics*, submitted.
2. "Use of a Measurement Model Technique for Analyzing EIS Data Quality from the Cathodic Reaction in SOFCs," J.R. Smith, M.E. Orazem and E.D. Wachsman, *Journal of the Electrochemical Society*, submitted.
3. "Three Dimensional Reconstruction of LSCF Cathodes," D. Gostovic, J.R. Smith, K.S. Jones and E.D. Wachsman, *Electrochemical and Solid State Letters*, submitted.

4. “Effect of Reduction Treatment on Fracture Properties of Cerium Oxide,” Y. Wang, K. Duncan, E. D. Wachsman, and F. Ebrahimi, *Journal of the American Ceramic Society*, submitted.
5. “Thermo-Chemical Expansion of Undoped and Gadolinium-Doped Cerium Oxide and Yttria Stabilized Zirconia,” S.R. Bishop, K. Duncan, and E. D. Wachsman, *Journal of the Electrochemical Society*, submitted.
6. “Deconvolution of SOFC Cathode Polarization,” E.D. Wachsman, *Solid Oxide Fuel Cells X, ECS Transactions*, K. Eguchi, S.C. Singhal and J. Mizusaki, Ed, accepted.
7. “The Effect of Point Defects on the Physical Properties of Non-Stoichiometric Oxides,” K. Duncan, Y. Wang, S.R. Bishop, F. Ebrahimi, and E. D. Wachsman, *Journal of Applied Physics*, accepted.
8. "General Model for the Functional Dependence of Defect Concentration on Oxygen Potential in Mixed Conducting Oxides," K. L. Duncan and E. D. Wachsman, *Ionics*, accepted.
9. “The Effect of Oxygen Vacancy Concentration on Elastic Modulus of Flourite-Structured Oxides,” Y. Wang, K. Duncan, E. D. Wachsman, and F. Ebrahimi, *Solid State Ionics*, **178**, 53-58 (2007).
10. “The Role of Point Defects in the Physical Properties of Fluorite Oxides,” K. L. Duncan, Y. Wang, S. R. Bishop, F. Ebrahimi, and E. D. Wachsman, *Journal of the American Ceramic Society*, **89**, 3162-3166 (2006).
11. “Thermo-Chemical Expansion of SOFC Materials,” S.R. Bishop, K.L. Duncan, and E. D. Wachsman, *Solid State Ionic Devices IV*, *ECS Transactions*, E.D. Wachsman, F.H. Garzon, E. Traversa, R. Mukundan, and V. Birss, Ed., **1-7**, 13-22 (2006).
12. “Effects of Oxygen Vacancy Concentration on Mechanical Properties of Cerium Oxide,” Y. Wang, K.L. Duncan, E. D. Wachsman, and F. Ebrahimi, *Solid State Ionic Devices IV*, *ECS Transactions*, E.D. Wachsman, F.H. Garzon, E. Traversa, R. Mukundan, and V. Birss, Ed., **1-7**, 23-34 (2006).
13. “Evaluation of Time Constants Governing the Cathodic Reactions in SOFCs,” J. R. Smith, M. Orazem, K. Duncan, A. Chen, and E. D. Wachsman, *Solid State Ionic Devices IV, ECS Transactions*, E.D. Wachsman, F.H. Garzon, E. Traversa, R. Mukundan, and V. Birss, Ed., **1-7**, 243-254 (2006).
14. “Effect of Harsh Anneals on the LSM/YSZ Interfacial Impedance Profile,” J. R. Smith and E. D. Wachsman, *Electrochimica Acta*, **51**, 1585-91 (2006).

REFERENCES

[1] A. Mitterdorfer, L. J. Gauckler, *Solid State Ionics* **111** (1998) 185.
[2] T. Horita, K. Yamaji, N. Sakai, H. Yokokawa, A. Weber and E. Ivers-Tiffée, *Solid State Ionics*, **133** (2000) 143.
[3] J. Crank, The Mathematics of Diffusion, *Oxford University Press,* (1980).
[4] B.C.H. Steele, *Solid State Ionics* **129** (2000) 95.
[5] P. S. Manning, J.D. Sirman, R.A. De Souza, *Solid State Ionics* **100** (1997) 1.
[6] D.K. Shetty, A.R. Rosenfield and W.H. Duckworth, *Eng. Fract. Mech.*, **26** (1987) 825.
[7] D. Singh and D. K. Shetty, *J. Am. Ceram. Soc.,* **72[1]** (1989) 78.
[8] C. Atkinson, R.E. Smelser and J. Sanchez, *Int. J. Fract.*, **18[4]** (1982) 279.
[9] F. A. Kroger and H. J. Vink, *Solid State Phys*. **3** (1956) 307.
[10] G. Brouwer, *Philips Res. Rep*. **9** 366-376 (1954).
[11] S. Wang, H. Inaba, H. Tagawa, M. Dokiya and T. Hashimoto, *Solid State Ionics* **107** (1998) 73.
[12] D. –J. Kim, *J. Amer. Cer. Soc*., **72** (1989) 1415.
[13] H. Inaba and H. Tagawa, *Solid State Ionics* **83** (1996) 1.
[14] H. L. Tuller and A. S. Nowick*, J. Electrochem. Soc.,* **126** (1979) 209.
[15] T. Otake, H. Yugami, K. Yashiro, Y. Nigara, T. Kawada and J. Mizusaki, *Solid State Ionics* **161** (2003) 181.
[16] S. Wang, T. Kobayashi, M. Dokiya and T. Hashimoto, *J. Electrochem. Soc.*, **147** (2000) 3606.
[17] B. C. H. Steele, *Solid State Ionics* **129** (2000) 95.
[18] M. Mogensen, N. M. Sammes and G. A. Tompsett, *Solid State Ionics* **129** (2000) 63.
[19] H. L. Tuller, chap. 6, pp 271-309 in "Nonstoichiometric Oxides," Edited by O. Sorensen, Academic, New York (1981).
[20] K. Duncan, *Ph. D. Thesis*, University of Florida (2001).
[21] E. Wachman and K. Duncan, "Stable High Conductivity Bilayered Electrolytes for Low Temperature SOFCs", *DOE Final Report*, **Contract No. DE-AC26-99FT40712** (2002).
[22] I. Riess, *J. Electrochem. Soc.* **128** (1981) 2077.
[23] M. Liu, *J. Electrochem. Soc.* **144** (1997) 1813.
[24] S. Yuan and U. Pal, *J. Electrochem. Soc.* **143** (1996) 3214.
[25] J. Newman, Electrochemical Systems (Prentice-Hall, 1991).
[26] P. J. Gellings, H. J. A. Koopmans and A. J. Burggraaf, *App. Catalysis* **39** (1988) 1.
[27] J.-W. Kim, A. V. Virkar, K.-Z. Fung, K. Mehta, and S. C. Singhal, *J. Electrochem. Soc*., **146** (1999) 69.
[28] S. R. Bishop, K. L. Duncan, E. D. Wachsman, "Thermo-Chemical Expansion of SOFC Materials," *ECS Trans.*, **1** (2006) 13.
[29] Keith L. Duncan, Yanli Wang, Sean R. Bishop, Fereshteh Ebrahimi, and Eric D. Wachsman *J. Appl. Phys*. **101** (2007) 044906.
[30] H.-W. Chiang, R. N. Blumenthal, and R. A. Fournelle, *Solid State Ionics*, **66** (1993) 85.
[31] Y. Wang, K. L. Duncan, E. D. Wachsman and F. Ebrahimi, *Solid State Ionics*, **178** (2007) 53.
[32] A. S. Wagh, R. B. Poeppel, J. P. Singh, *J. Mater. Sci.*, **26** (1991) 3862.

[33] A. Atkinson, *Solid State Ionics* **95** (1997) p. 249.
[34] K. Sato, H. Yugami and T. Hashida *J. Mater. Sci.* **61** (1999), 5765.
[35] B. Savoini, D. Cáceres, I. Vergara, *et.al*., *J. of Nuclear Materials* **277** (2000), 199.
[36] J. W. Adams, R. Ruh, K. S. Mazdiyasni, *J. Am. Ceram. Soc*. **80** (1997), 903.
[37] A. J. A.Winnubst, K. Keizer and A. J. Burggraaf, *J. Mater. Sci.* **18** (1983), 1996.
[38] K. Duncan, Y. Wang, S. Bishop, F. Ebrahimi, and E. D. Wachsman, *J. Am. Ceram. Soc.*, **89** (2006) 3162.
[39] S. Wang, M. Katsuki, T. Hashimoto, *J. Elecctrochem. Soc.* **150** (2003) A952.
[40] D. J. M. Bevan and J. Kordis, *J. Inorg. Nucl. Chem.* 26 (1964), 1509.
[41] A. A. Griffith, *Phil. Trans. Roy. Soc. Lond.*, **A221** (1920), 163.
[42] Y. Wang, K. Duncan, E. Wachsman and F. Ebrahimi, *Solid State Ionics,* **178** (2007) 53.
[43] K. T. Faber and A. G. Evans, *Acta Metall.,* **31** (1983) 565.
[44] K.T.Faber and A.G. Evans, *Acta Metall.,* **31[4]** (1983) 577.
[45] J. W. Hutchinson, *Acta Metall.,* **35** (1987) 1605.
[46] M. Rühle, A. G. Evans, R. M. McMeeking P. G. Charalambides and J. W. Hutchinson, *Acta Metall.,* **35** (1987) 2701.
[47] A. G. Evans and K. T. Faber, *J. Am. Ceram. Soc.,* **67** (1984) 255.
[48] C. K. Chen, *J. Eur. Ceram. Soc.*, **25** (2005) 3293.
[49] M. E. Orazem, *J. Electroanalyt. Chem*., **572** (2004) 317.
[50] A. Mitterdorfer and L. J. Gauckler, *Solid State Ionics*, **117** (1999) 203.
[51] X. Guo and A. Maier, *J. Electrochem. Soc*., **148** (2001) E121.
[52] S. Adler, *Chemical Reviews*, **104** (2004) 4791.
[53] J. R. Smith, A. Chen, D. Gostovic, D. Hickey, D. Kundinger, K. L. Duncan, R. T. DeHoff, K. S. Jones and E. D. Wachsman, *Solid State Ionics*, submitted.
[54] D. Gostovic, J. R. Smith, K. S. Jones and E. D. Wachsman, *Electrochemical and Solid State Letters*, submitted.